Politecnico di Torino

Politecnico di Torino

Master's Degree in Aerospace Engineering

Academic Year 2025/2026

Thermal Modeling of the ROMEO Satellite with a Focus on the Langmuir Probe Instrument

Supervisors

Paolo Maggiore

Matteo Davide Lorenzo Dalla Vedova

External Supervisor

Mykola Ivchenko

KTH Royal Institute of Technology

Candidate

Giuditta Marvulli

Degree Project in Electrical Engineering, specialising in Electromagnetics, Fusion and Space Engineering

Second cycle, 30 credits

Thermal Modeling of the ROMEO Satellite with a Focus on the Langmuir Probe Instrument

Stockholm, Sweden 2025

GIUDITTA MARVULLI

Author

Giuditta Marvulli
KTH Royal Institute of Technology

Supervisor

Mykola Ivchenko - KTH Royal Institute of Technology

Examiner

Lorenz Roth - KTH Royal Institute of Technology

Collaborators

Antonie Käufl - University of Stuttgart
Michael Lengowski - University of Stuttgart

Academic Referees (Home University)

Paolo Maggiore - Polytechnic University of Turin

Matteo Davide Lorenzo Dalla Vedova - Polytechnic University of Turin

Abstract

This thesis focuses on the thermal modeling of the Langmuir instrument developed by the Royal Institute of Technology for the Research and Observation in Medium Earth Orbit (ROMEO) satellite. The ROMEO satellite is part of the University of Stuttgart's small satellite program, developed to test cost-efficient space technologies in Low Earth Orbit (LEO) and Medium Earth Orbit (MEO). The deployable Langmuir probes measure the thermal plasma environment and its interaction with the satellite's water propulsion system.

Using the well-established tool for spacecraft thermal analysis, Systema-Thermica, the project aims to study the thermal behaviour of the instrument, ensuring optimal performance during its lifetime in the harsh conditions of space. To achieve this, a simplified model of the ROMEO satellite, derived from the complete version provided by the University of Stuttgart, was developed. The simplification focuses the analysis on the Langmuir Probe instrument by removing unnecessary components, thereby significantly reducing computational time. The purpose of this study is to validate the adopted approach and assumptions, with simulations performed under worst-case thermal scenarios. Simulation results show that, under worst-case hot conditions, the instrument remains within operational temperature limits, while in the cold case, the booms and probes fall below the minimum threshold, highlighting the need for further investigation or thermal control measures. Moreover, the results from the simplified model were found to be in good agreement with those obtained using the full satellite model, supporting the effectiveness of the proposed methodology.

Keywords

Thermal modeling, Thermica, ROMEO satellite, Langmuir Probe, Langmuir Electronics, Temperature, Simulations.

Sammanfattning

Denna avhandling fokuserar på termisk modellering av Langmuir-instrumentet som drivs av Kungliga Tekniska Högskolan ombord på satelliten ROMEO. Satelliten ROMEO är en del av Stuttgarts universitets program för små satelliter, som utvecklats för att testa kostnadseffektiva rymdtekniker i LEO och MEO. De utfällbara Langmuir-sonderna mäter den termiska plasmamiljön och dess interaktion med satellitens vattenpropulsionssystem.
Med hjälp av det väl etablerade verktyget för termisk analys av rymdfarkoster, Systema-Thermica, syftar projektet till att studera instrumentets termiska beteende för att säkerställa optimal prestanda under dess livstid i rymdens tuffa förhållanden. För att uppnå detta har en förenklad modell av satelliten ROMEO utvecklats, baserad på den fullständiga versionen från universitetet i Stuttgart. Förenklingen fokuserar analysen på Langmuir-sondinstrumentet genom att ta bort onödiga komponenter, vilket avsevärt minskar beräkningstiden. Syftet är att presentera och validera den antagna metoden och antagandena med simuleringar utförda under värsta tänkbara termiska scenarier. Simuleringsresultaten visar att instrumentet under värsta tänkbara värmeförhållanden håller sig inom driftstemperaturgränserna, medan det i kalla förhållanden faller under minimitröskeln, vilket understryker behovet av ytterligare undersökningar eller åtgärder för termisk kontroll. Dessutom visade sig resultaten från den förenklade modellen stämma väl överens med de resultat som erhölls med hjälp av den fullständiga satellitmodellen, vilket styrker effektiviteten i den föreslagna metoden.

Nyckelord

Termisk modellering, Thermica, ROMEO-satellit, Langmuir-sonder, Langmuir-Elektronik, Temperatur, Simuleringar.

Acknowledgements

I would like to thank my supervisor, Mr.Mykola Ivchenko, for his continuous support and guidance throughout the thesis work. His expertise and optimism have been essential to completing this work successfully.

I would also like to thank my examiner, Mr.Lorenz Roth, for his availability throughout the evaluation process.

I want to express my gratitude to my supervisors from Politecnico di Torino, Mr. Paolo Maggiore and Mr. Matteo Davide Lorenzo Dalla Vedova, for supporting me in this project abroad.

I am very grateful to the Stuttgart team, Mr.Michael Lengowski and Ms.Antonie Käufl, for their input and encouragement. In particular, Antonie Käufl has provided continuous help in understanding the previous work done and the Systema-Thermica environment.

I would like to thank the KTH ROMEO team for creating an exciting and inspiring environment.

Furthermore, I would also like to thank my colleagues and friends, Mr.Antonino Mangano and Mr.Mattia Tadiotto, for their emotional and technical support throughout this year at KTH.

Finally, I want to express my profound gratitude to my family, my friends, and my boyfriend for providing invaluable support during my entire academic journey. This accomplishment would not have been possible without them. Thank you.

Contents

List of Figures

List of Tables

Acronyms

Al	Aluminium
AU	Astronomical Unit
BOL	Beginning of Life
CFRP	Carbon Fiber Reinforced Polymer
DDS	Data-dowlink with S-band
EOL	End of Life
FEP	Fluorinated Ethylene Propylene
IRS	Institute of Space Systems
IR	Infrared Radiation
KTH	Royal Institute of Technology
LEO	Low Earth Orbit
LTAN	Local Time of Ascending Node
MEO	Medium Earth Orbit
MLI	Multi-Layer Insulation
MST	Mean Solar Time
OSRs	Optical Solar Reflectors
PCMs	Phase-Change Materials
RCN	Reduced Conductive Network
REF	Radiation Exchange Factor
ROMEO	Research and Observation in Medium Earth Orbit
SS	Stainless Steel
TST	True Solar Time
UV	Ultraviolet
VBA	Visual Basic for Applications

Chapter 1

Introduction

ROMEO is a space mission designed by Institute of Space Systems (IRS) at the University of Stuttgart, which intends to launch a 60 kg satellite into a Sun-synchronous LEO with an altitude of 600 km [14]. The satellite will carry a propulsion system to increase its apogee above 2,000 km, while lowering the perigee, and the nominal mission duration is 1 year. In contrast to the relatively protected LEO, the radiation environment in the orbits passing the Van Allen radiation belt is quite problematic for electronic components. The ROMEO platform aims to show that MEO can be an operational area for small satellite missions using commercial components. Furthermore, ROMEO's scientific payloads will be utilized to study parameters related to Earth's climate change and space weather phenomena. In fact, because of its elliptical orbit, the ROMEO satellite orbits both the ionosphere and the inner radiation belt, where it can detect changes in space weather.

The Royal Institute of Technology (KTH) in Stockholm develops a Langmuir instrument on the ROMEO satellite, measuring the thermal plasma environment in the area surrounding the satellite and its interaction with the fuel of the new development water-propulsion system. For this purpose, two deployable Langmuir probes, attached to the satellite's fold-out solar panels, are implemented to analyze electron density, electron temperature, and plasma potential.

The space is an extremely harsh environment when it comes to radiation, vacuum, and temperature. The satellite faces the dual challenges of intense solar heating, where temperatures can reach several hundred degrees Celsius, and the frigid cold of deep space, where it is approximately 2.7 K [5]. Due to these fluctuations in temperature,

it is important to predict and mitigate these thermal challenges, ensuring optimal subsystem performance.

The investigation conducted in this thesis focuses on the methodology and validity of using a simplified model to analyze the thermal behavior of the Langmuir instrument under extreme space environmental conditions through simulations in Systema-Thermica, aiming to reduce computational time while preserving the accuracy of the results. The results are evaluated to verify whether the predicted temperatures remain within the instrument's operational range, ensuring its performance. The validity of the simplified approach is then assessed through a comparison with the complete version of the ROMEO thermal model provided by the University of Stuttgart.

Chapter 2

Background

This chapter presents the background required to understand the thermal processes that occur in a satellite, as well as the various factors that influence them. To support this, a fundamental overview of thermodynamics, the space environment, and satellite technologies is provided.

2.1 Heat transfer theory

Heat transfer is defined as the thermal energy that is transferred from one system to another system as a result of temperature differences. There are three modes of heat transfer: convection, conduction, and radiation.

2.1.1 Convection

Convection is defined as the heat exchange because of the (bulk) motion of fluids or gases, which can be neglected due to the vacuum condition in space.

2.1.2 Conduction

Conduction is defined as the transfer of heat due to microscopic collisions between particles. This includes the phenomena both within a body as well as between two contacting bodies, without the displacement of matter. The principle of heat conduction is governed by Fourier's law, which states that the conduction heat rate $\dot{q}$ in per unit area is proportional to the gradient of the temperature T in the direction normal to the area:

$$\dot{q}(x, y, z, t) = -k\nabla T \tag{2.1}$$

where k is the proportionality factor known as thermal conductivity, given in W/(m·K). It is also a function of temperature, but within the temperature ranges involved in this report, it can be considered constant. The minus sign indicates the direction of heat flow, ensuring that it occurs toward a lower temperature. In the stationary, one-dimensional case, Fourier's law can be simplified as

$$\dot{q} = -k\frac{dT}{dx}. \tag{2.2}$$

Considering a body with area A (m²) and conducting length L (m), it results in:

$$\dot{q} = \frac{\dot{Q}}{A} = -k\frac{(T2 - T1)}{L} \tag{2.3}$$

where $T2$ (K), $T1$ (K) are the temperatures and $\dot{Q}$ (W) is the heat flowing through the area A. Since the thermal conductivity k, the area A, and the conductive length L are constant factors, they can be summarized as the so-called thermal resistance R [9]:

$$R = k\frac{A}{L}. \tag{2.4}$$

Conductors through multiple components with different thermal conductivities can be considered as series (illustrated in Figure 2.1) or parallel connections. In a series, the resistance is determined by the sum of the individual resistance of the same area A:

$$R = \sum_{i=1}^{n} R_i. \tag{2.5}$$

In parallel, the reciprocal of the resistance is determined by the sum of individual resistances of the same area A:

$$\frac{1}{R} = \sum_{i=1}^{n} \frac{1}{R_i}. \tag{2.6}$$

Since in reality heat transfer is not ideal, a contact resistance R_c is introduced, which accounts for the heat transfer coefficient h_c (W·m^{-2}·K^{-1}). This coefficient is typically obtained from experimental data or literature values, as it depends on several factors, including surface roughness, type of mechanical connection, contact pressure, and presence of interface materials or fillers [7]. The contact resistance is expressed

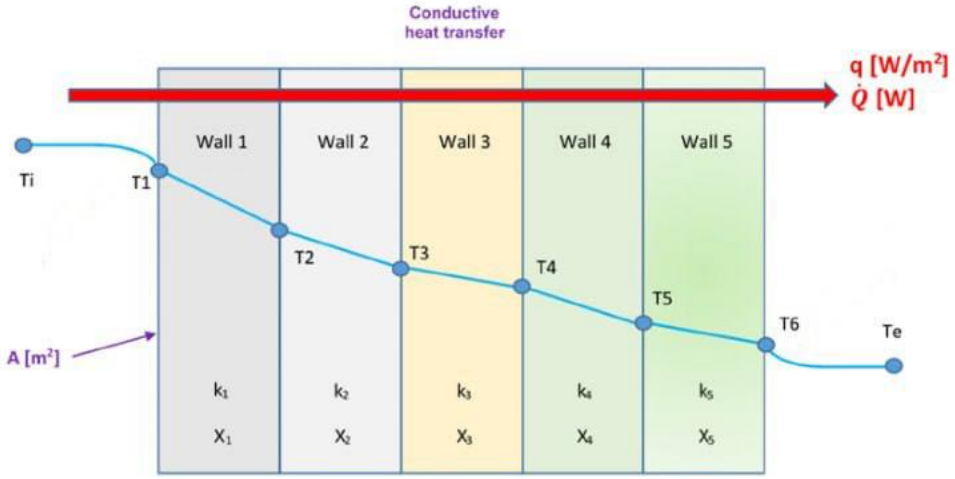

Figure 2.1: Heat transfer through a multilayer wall with series connection. Adapted from [12].

as

$$R_c = \frac{1}{h_c A}. \tag{2.7}$$

An important parameter in the implementation of thermal simulations is the inverse of thermal resistance, referred to as thermal conductance, denoted as GL (W·K^{-1})[7].

In the thermal software, the model is discretized into nodes, and the conductive couplings are used to describe how the heat is transferred from one node to another. Considering two nodes B_1 and B_2, the conductive coupling between them, illustrated in Figure 2.2, is given by

$$GL_{B_1->B_2} = \frac{1}{\frac{1}{G_{B_1}} + \frac{1}{h_c A} + \frac{1}{G_{B_2}}} \tag{2.8}$$

where A is the surface contact between node B_1 and B_2, and

$$G_j = \frac{k_j A_j}{L_j} \tag{2.9}$$

where A_j is the cross-sectional area of node j, k_j is the thermal conductivity, and L_j is the distance traversed by the heat from the middle of node j to the boundary [5]. If there are no interfacing contact surfaces, the middle term in the denominator can be neglected.

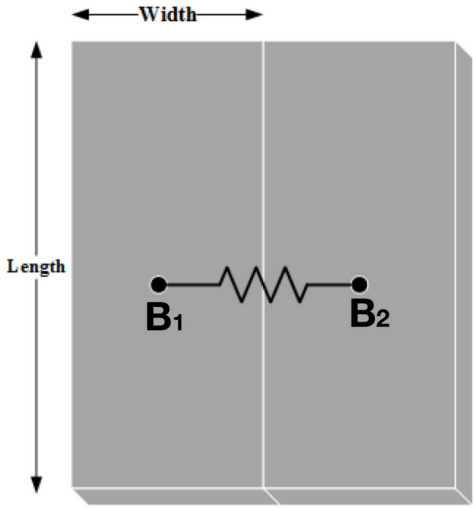

Figure 2.2: Conductive coupling between two nodes. Adapted from [6]

2.1.3 Radiation

Radiation is the energy emitted by matter in the form of electromagnetic waves as a result of changes in the electronic configurations of the atom or molecules. It represents a conversion from thermal energy to electromagnetic energy. All bodies with a temperature higher than absolute zero emit thermal radiation. An ideal body that absorbs all incident radiation without any reflection or transmission is known as a blackbody. Its spectral radiance, $I(\lambda, T)$ $(\mathrm{W} \cdot \mathrm{sr}^{-1} \cdot \mathrm{m}^{-2} \cdot \mathrm{nm}^{-1})$, is described by Planck's radiation law as

$$I(\lambda, T) = \frac{2hc^2}{\lambda^5} \frac{1}{e^{\frac{hc}{\lambda k T}} - 1} \tag{2.10}$$

where λ (m) is the wavelength, T (K) is the surface temperature, h $(\mathrm{J} \cdot \mathrm{s}^{-1})$ is Planck's constant, which describes the relationship between the energy of a photon and its frequency, c $(\mathrm{m} \cdot \mathrm{s}^{-1})$ is the speed of light in vacuum, k $(\mathrm{J} \cdot \mathrm{K}^{-1})$ is the Boltzmann constant, which describes the relationship between temperature and the kinetic energy. As the temperature of a body increases, its total emitted radiation also increases, and the peak of its emission spectrum shifts toward shorter wavelengths. This behavior is described by Wien's displacement law, which defines the wavelength at which the emission reaches its maximum as

$$\lambda_{peak} = \frac{2.898 \cdot 10^{-3}}{T} \tag{2.11}$$

where $2.898 \cdot 10^{-3}$ $(\mathrm{m} \cdot \mathrm{K})$ is Wien's displacement constant.

From the integration of Planck's radiation law 2.10 over all wavelengths, the power radiated P (W/m²) from a blackbody is obtained. It is described by the Stefan-Boltzmann law as

$$P = \sigma \cdot T_{surface}^4 \tag{2.12}$$

where $\sigma = 5.670 \cdot 10^{-8}$ (W $\cdot$ m^{-2} $\cdot$ K^{-4}) is the Stefan-Boltzmann constant, and T (K) is the temperature of the body. In reality, only a part of the radiation is emitted. For a non-ideal radiator, so-called gray body, the power radiated P (W/m²) is given by

$$P = \varepsilon \cdot \sigma \cdot T^4 \tag{2.13}$$

where ε is the emission coefficient (emissivity) that varies in the interval $0 \leq \varepsilon \leq 1$, and depends on the properties of the surface. The emissivity indicates how closely a surface behaves like an ideal blackbody, which has $\varepsilon = 1$.

The heat $\dot{Q}$ (W) radiated by a body is given by the power radiated P (W/m²) multiplied by the emitting area A_e (m²), which gives

$$\dot{Q} = \varepsilon \cdot \sigma \cdot T^4 \cdot A_e. \tag{2.14}$$

Another important parameter is the absorptivity α, which is the fraction of the incident radiation energy absorbed by the surface. It determines the absorbed heat flux according to:

$$\dot{q}_{abs} = \alpha \dot{q}_{inc}. \tag{2.15}$$

Emissivity and absorptivity are thermo-optical properties of materials that play a crucial role in the thermal design of a spacecraft, as they directly influence its radiative heat exchange. These properties can change over the operational lifetime of the satellite due to material degradation, which is why the thermal behavior of the spacecraft is typically evaluated under two conditions: Beginning of Life (BOL) and End of Life (EOL).

When radiation strikes a body, it is generally divided into three components: a portion is reflected from the surface (described by the reflectance ρ), another portion is transmitted through the material (described by the transmittance τ), and the remaining part is absorbed and converted into internal energy (described by the absorptivity α). These three components account for the entire incident radiation and

satisfy the following balance: $\alpha + \rho + \tau = 1$. For an opaque surface (i.e., $\tau = 0$), the relation between the spectral directional hemispherical reflectance $\rho_\lambda(\phi, \theta)$[1], spectral directional emittance $\varepsilon_\lambda(\phi, \theta)$, and the spectral directional absorptance $\alpha_\lambda(\phi, \theta)$, is then given by Kirchhoff's first thermal law:

$$\alpha_\lambda(\phi, \theta) = \varepsilon_\lambda(\phi, \theta) = 1 - \rho_\lambda(\phi, \theta). \tag{2.16}$$

For simplification in calculations, surfaces are often modeled as Lambertian radiators [13]. A Lambertian surface emits and reflects radiation diffusely and uniformly in all directions, meaning the directional dependence of radiation intensity can be neglected. Moreover, it is typically assumed to be opaque to radiation, so that, at a given wavelength λ (m) and temperature T (K), the spectral emissivity ε is equal to the spectral absorptivity α:

$$\varepsilon(\lambda, T) = \alpha(\lambda, T). \tag{2.17}$$

To evaluate the radiative exchange between multiple bodies, view factors are required. The view factor (or form factor) describes the fraction of radiated energy emitted by an element 1 that is intercepted by an element 2.

$$F_{1\to2} = \frac{\Phi_{1\to2}}{\Phi_1} \tag{2.18}$$

where Φ_1(W) is the radiation flux from surface A_1(m²), and $\Phi_{1\to2}$(W) is the portion of Φ_1 that hits surface A_2(m²), depending on the geometry and orientation [9]. Taking into account the two surfaces shown in Figure 2.3 that have differential areas dA_1 and dA_2, and defining $I_1(\mathrm{W} \cdot \mathrm{m}^{-2} \cdot \mathrm{sr}^{-1})$ as the intensity of what surface dA_1 emits and reflects. Considering that this intensity is constant in all directions for the Lambertian radiator[2], the portion of radiation that leaves dA_1 and hits dA_2 is given by

$$d\Phi_{1\to2} = I_1 \cos\theta_1 dA_1 d\omega_{21} = I_1 \cos\theta_1 dA_1 \frac{dA_2 \cos\theta_2}{s^2} \tag{2.19}$$

where $d\omega_{21}$ is the solid angle subtended by dA_2 when viewed by dA_1, s is the distance between the two surfaces, θ_1 and θ_2 are respectively the angles between the surface normals (n_1 and n_2) and the line s [4]. The differential view factor $dF_{1\to2}$ is then

[1] $\rho_\lambda(\phi, \theta)$ is the reflectance at all angles from a monochromatic beam incident from the direction (ϕ, θ).

[2] For a Lambertian radiator $d\Phi_1 = \pi I_1 dA_1$. This relationship arises from integrating the radiative intensity over the hemisphere above the surface, considering the cosine angular dependence of diffuse emission.

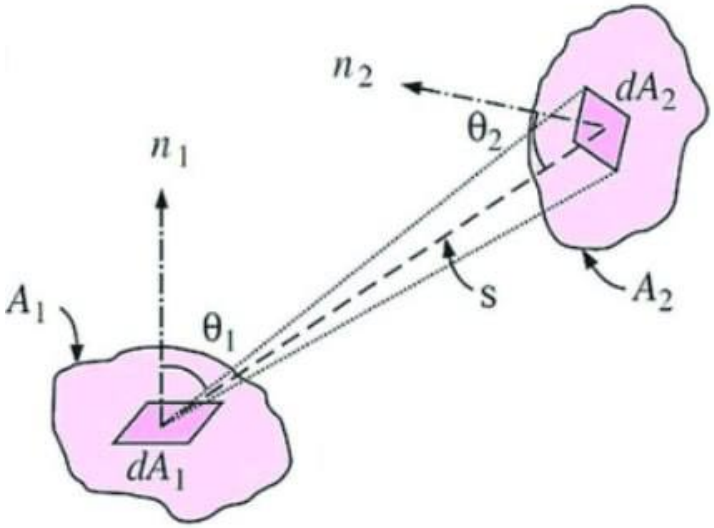

Figure 2.3: Geometry for the view factors calculation [15].

calculated as

$$dF_{1\to 2} = \frac{\cos\theta_1 \cos\theta_2}{\pi s^2} dA_2. \tag{2.20}$$

The exact solution is given by

$$F_{1\to 2} = \frac{1}{A_1} \int_{A_1} \int_{A_2} \frac{\cos\theta_1 \cos\theta_2}{\pi s^2} dA_2 dA_1. \tag{2.21}$$

When the surfaces are considered in reverse, the reciprocity principle applies:

$$dF_{1\to 2} dA_1 = dF_{2\to 1} dA_2. \tag{2.22}$$

which for finite surfaces becomes

$$F_{1\to 2} A_1 = F_{2\to 1} A_2. \tag{2.23}$$

The heat flow between two surfaces can be calculated as

$$\dot{Q}_{1\to 2} = \Phi_{1\to 2} - \Phi_{2\to 1} = F_{1\to 2}\varepsilon_1 A_1 \sigma T_1^4 - F_{2\to 1}\varepsilon_2 A_2 \sigma T_2^4. \tag{2.24}$$

The view factor can be summarized in the radiative coupling $GR_{B_1\to B_2}$ (W/K^4) between two nodes B_1 and B_2, known as Radiation Exchange Factor (REF) and expressed as

$$GR_{B_1\to B_2} = \varepsilon_{B_1} D_{B_1\to B_2} A_{B_1} \tag{2.25}$$

where ε_{B_1} is the emissivity of the node B_1, $D_{B_1 \to B_2}$ is the Gebhart factor from B_1 to node B_2, and A_{B_1} is the area of the node B_1 [5]. The Gebhart factor is defined as the fraction of energy leaving node B_1 that is absorbed at node B_2, and it accounts for the radiative view factor between all nodes seen by node B_1. The radiative couplings, along with the view factors and Gebhart factors, are computed automatically within Systema-Thermica.

2.2 Space thermal environment

Spacecraft are subject to challenging thermal conditions in space, primarily resulting from external sources such as direct solar radiation with an average solar constant of 1367 (W/m²), Earth's reflected sunlight (albedo), and its emitted IR, illustrated in Figure 2.4. Furthermore, during eclipses or on the side facing away from the Sun, the

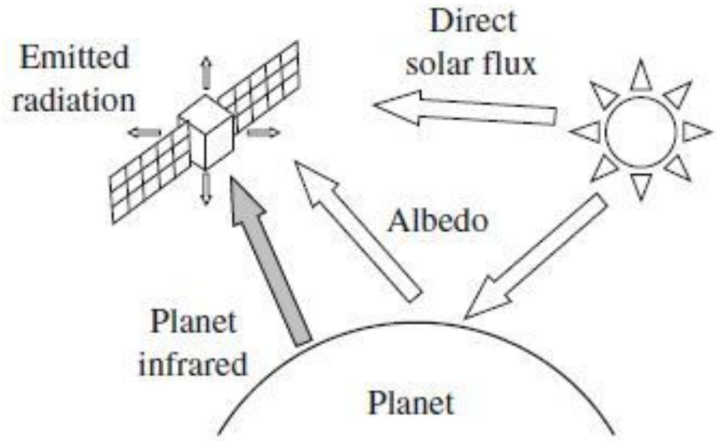

Figure 2.4: Space environment [11].

satellite faces very low temperatures, as it is exposed only to the background radiation of space at approximately -270 °C. The thermal balance of the spacecraft is also influenced by internal factors, such as the heat generated by the power dissipation of electrical components. These conditions, influenced by orbital parameters, attitude, and mission timeline, result in a dynamic thermal environment that causes the spacecraft to undergo temperature fluctuations.

2.2.1 Solar Radiation

Solar radiation is the satellite's main source of heat, and its intensity varies with the distance between the Earth and the Sun. Due to the elliptical shape of Earth's orbit,

the received solar intensity changes throughout the revolution around the Sun: during the summer solstice, Earth is near aphelion (farthest from the Sun), and the solar constant decreases to approximately 1322 $(\mathrm{W/m^2})$; at the winter solstice, Earth is near perihelion (closest to the Sun), and the intensity increases to about 1414 $(\mathrm{W/m^2})$ [4]. The heat transfer $\dot{Q}_{B_1,s}$ (W) from the solar radiation to a node B_1 is then given by

$$\dot{Q}_{B_1,s} = \alpha_{B_1} S_s A_{B_1} \tag{2.26}$$

where α_{B_1} is the absorptivity of the node, A_{B_1} is the area of the node, and $S_s(\mathrm{W/m^2})$ is the constant solar flux, defined as the amount of solar radiation per unit area received on a surface perpendicular to the Sun's rays at a distance of 1 Astronomical Unit (AU) [6].

2.2.2 Earth Albedo

The albedo is the fraction of solar radiation reflected by the Earth's surface and atmosphere back into space. The average albedo observed is around 30% but its value depends on several factors. Typically, continental regions exhibit higher reflectivity than oceanic areas, due to differences in surface composition and texture. Moreover, albedo increases when the local solar elevation angle decreases, meaning that surfaces reflect more sunlight when the Sun is low on the horizon. Similarly, cloud cover significantly enhances albedo, as clouds are highly reflective and scatter incoming solar radiation. Surfaces covered with snow or ice also reflect a substantial portion of incoming sunlight, further raising the local albedo. As a result, regions with high latitudes, frequent cloud coverage, or persistent snow and ice tend to have higher overall albedo values. From the perspective of a spacecraft, the albedo flux it receives depends on its position relative to the sub-solar point, the point on Earth where the Sun is directly overhead. As the spacecraft moves away from this point, the intensity of reflected radiation it receives decreases, due to the lower solar incidence and greater path length through the atmosphere. The thermal energy transferred $\dot{Q}_{B_1,a}$ (W) to a node B_1 as a result of the Albedo can be expressed as

$$\dot{Q}_{B_1,a} = \alpha_{B_1} S_s a A_{B_1} \frac{R_E^2}{(R_E + h)^2} \tag{2.27}$$

where a is Albedo constant, which represents the effective fraction of solar radiation reflected by the Earth that reaches a particular surface of the spacecraft, R_E is Earth's radius, and h is the altitude of the spacecraft.

2.2.3 Earth IR

All solar radiation incident on the Earth's surface that is not reflected as albedo is absorbed by the Earth and eventually re-emitted as thermal IR. The Earth radiates with an average temperature -18 °C [9], which gives a maximum wavelength in the infrared range due to Equation (2.11). In general, the intensity of IR primarily depends on the local surface temperature of the Earth and the presence of clouds. Warmer regions emit more infrared radiation, while colder areas emit less. However, cloud coverage plays a significant role: even in warm regions, a high density of clouds can reduce the outgoing IR intensity, as clouds tend to absorb and scatter thermal radiation [6]. The thermal energy transferred $\dot{Q}_{B_1,IR}$ (W) to a node B_1 as a result of the Earth IR can be expressed as

$$\dot{Q}_{B_1,IR} = \varepsilon_{B_1} S_{IR} A_{B_1} \frac{R_E^2}{(R_E + h)^2} \tag{2.28}$$

where ε_{B_1} is the emissivity of the node B_1, S_{IR} (W/m²) is the Earth IR flux, whose average value observed is 236 W/m².

2.2.4 Heat Capacity

Heat capacity C (J/K) quantifies the thermal energy required to raise the temperature of a body by 1 K. It is formally defined as

$$C = \frac{dQ}{dT}. \tag{2.29}$$

Considering a specific thermal node B_1, the heat capacity can be written as

$$C_{B_1} = c_{sp} \rho_{B_1} V_{B_1} \tag{2.30}$$

where ρ_{B_1} (kg/m³) is the density of the node, V_{B_1} (m³) is its volume, and c_{sp} ($\mathrm{J \cdot kg^{-1} \cdot K^{-1}}$) is the specific heat capacity (heat capacity divided by the mass).

2.2.5 Thermal energy balance

The comprehensive thermal balance of a satellite can be obtained by managing the energy transmitted by the satellite against the energy received from the external environment, plus the energy dissipated by the internal electronic components.

$$C\frac{dT}{dt} = \dot{Q}_{in} - \dot{Q}_{out} = \dot{Q}_s + \dot{Q}_a + \dot{Q}_{IR} + \dot{Q}_I - \dot{Q}_R \tag{2.31}$$

where t is the time, and the different power sources are:

- $\dot{Q}_s$ is the solar radiation;
- $\dot{Q}_a$ is the albedo radiation;
- $\dot{Q}_{IR}$ is the IR;
- $\dot{Q}_I$ is the internal heat dissipation of the components;
- $\dot{Q}_R$ is the radiated power from the satellite.

2.3 Numerical methods

Numerical methods are adopted because the complexity of the differential equation (Equation (2.31)) makes analytical solutions impractical. The simulation software performs the numerical calculation by simplifying the system, allowing the resulting temperature to be determined.

2.3.1 Node Network

The idea behind the numerical methods is to divide the system into so-called nodes, which are defined as subvolumes or surfaces within which a uniform temperature is assumed. The geometry of the physical body is represented by surfaces, which are then discretized into multiple nodes. Each node is positioned at the center of a subarea and is assigned geometric and physical properties, such as area, thickness, specific heat capacity, and density in order to compute its mass and, consequently, its heat capacity, as expressed in Equation (2.30). Each node is thermally connected to the others through conductive couplings (according to Equation (2.8)) and REF (according to Equation (2.25)). Therefore, thermal conductivity, absorptivity, and

emissivity must be defined.[3] As a result of this nodal discretization and the associated thermal couplings, the heat balance equation (Equation (2.31)) for a single node i can be expressed as

$$C_i \frac{dT_i}{dt} = \sigma \sum_{i \neq j} GR_{ij}(T_j^4 - T_i^4) + \sum_{i \neq j} GL_{ij}(T_j - T_i) + \dot{Q}_{in,i}. \tag{2.32}$$

View factors are computed using the Monte Carlo ray tracing method, a numerical technique that involves stochastic elements [9]. From a randomly selected point on a surface i, a ray is emitted in a random direction. It is then checked whether the ray hits a surface j. This process is repeated many times for each surface, and the view factor between surfaces i and j is estimated as the ratio of rays that reach surface j to the total number of rays emitted from surface i. The accuracy of the result improves with the number of emitted rays, but this comes at the cost of increased computational effort.

2.3.2 Crank–Nicolson Method

To solve the system of heat balance equations derived from the nodal discretization, the Crank–Nicolson method is used [9]. This method offers second-order accuracy in both time and space and is unconditionally stable, making it suitable for time-dependent thermal problems. It is commonly formulated as

$$\frac{u_i^{n+1} - u_i^n}{\Delta t} = k \frac{u_{i+1}^{n+1/2} - 2u_i^{n+1/2} + u_{i-1}^{n+1/2}}{\Delta x^2} \tag{2.33}$$

where u_i^n represents the temperature at node i and time step n, Δx represents the space step and Δt the time step, and $u_i^{n+1/2}$ is the arithmetic average between two consecutive time steps:

$$u_i^{n+1/2} = \frac{1}{2}(u_i^n + u_i^{n+1}) \tag{2.34}$$

Applying this to the balance equation (Equation (2.32)), the calculation for each node

[3] Absorptivity and emissivity are wavelength-dependent. The peak of the Sun's spectral radiation lies in a different wavelength range than that of the thermal radiation emitted by the body. As a result, ε_{IR}, which equals α_{IR} in accordance with Equation (2.17), is used for the body's infrared emission and for the absorption of Earth's IR. Conversely, α_{UV} is used, by convention, for the absorption of solar and albedo radiation, whose energy is primarily distributed across the Ultraviolet (UV), visible, and near-infrared spectrum, with the peak in the visible range.

of the system of equation is expressed as

$$
\begin{aligned}
C_i \frac{T_i^{n+1} - T_i^n}{\Delta t} = & \sum_{i \neq j} GL_{ij} \left(\frac{T_j^{n+1} + T_j^n}{2} - \frac{T_i^{n+1} + T_i^n}{2} \right) \\
& + \sigma \sum_{i \neq j} GR_{ij} \left(\frac{(T_j^{n+1})^4 + (T_j^n)^4}{2} - \frac{(T_i^{n+1})^4 + (T_i^n)^4}{2} \right) \\
& + \frac{\dot{Q}_i^{n+1} + \dot{Q}_i^n}{2}.
\end{aligned}
\tag{2.35}
$$

2.4 ROMEO mission

ROMEO is a space mission initiated by the IRS at the University of Stuttgart. Its main goal is to develop a low-cost satellite platform capable of testing new technologies in both LEO and MEO. The mission involves launching a 60 kg satellite into a sun-synchronous orbit at an altitude of 600 km. After reaching this orbit, the satellite's apogee will be raised above 2000 km using a water-based propulsion system. This innovative technology works by splitting water into hydrogen and oxygen via electrolysis, which are then recombined in a chemical bi-propellant to produce thrust. A key aspect of ROMEO is to prove that MEO is operable for small satellite missions using commercial off-the-shelf components. Unlike the relatively safe environment of LEO, MEO exposes satellites to much harsher radiation levels, especially while crossing the Van Allen belts.

ROMEO's onboard instruments will be used to observe and analyze data related to climate change on Earth and space weather conditions. In addition to standard solar panels, ROMEO is equipped with perovskite solar cells, an emerging photovoltaic technology made of minerals with a unique crystal structure. This experiment aims to test different crystal compositions. Perovskite cells offer promising advantages, including higher efficiency, a superior power-to-mass ratio, enhanced radiation resistance, and low-cost manufacturing. To optimize mass efficiency, ROMEO's primary structure uses a sandwich design: an aluminum honeycomb core enclosed between two quasi-isotropic Carbon Fiber Reinforced Polymer (CFRP) panels. The satellite is divided into three main levels, shown in Figure 2.5.

- The lower level, which contains the service module, housing avionics units, and the battery.

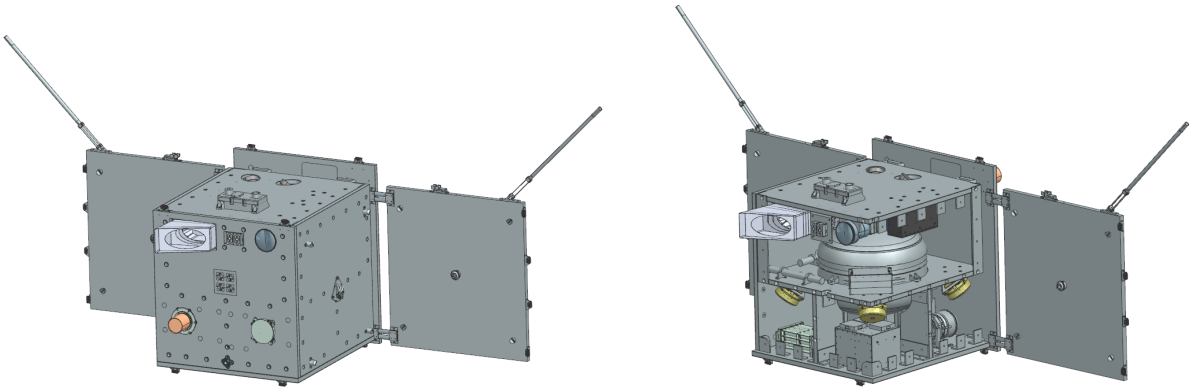

Figure 2.5: ROMEO satellite CAD model.

- The upper level, which holds the payload module, including the electrolyzer and engine. This upper module also supports the Earthshine telescope[4], cameras, a particle detector, space weather sensors, and the plasma sensor electronics.
- The core module, which hosts the water tank, reaction wheels, magnetic torquers for attitude control, the perovskite electronics, and the Langmuir electronics.

The ROMEO mission is planned to last one year and is divided into three phases to ensure a high success rate while operating in the radiation belt:

- In Phase 1, the satellite is launched into a Sun-synchronous orbit at 600 km, chosen because of frequent ride-sharing opportunities for small satellites. During this phase, climate studies are carried out using the Earthshine Telescope.
- In Phase 2, the spacecraft uses its water propulsion system to raise its apogee above 2,000 km, a maneuver that takes around 140 days.
- In Phase 3, the satellite reaches its final orbit of 2500 × 330 km to perform research on the inner radiation belt. The lower perigee ensures compliance with the European Code of Conduct for Space Debris Mitigation, allowing for atmospheric reentry within 25 years.

Langmuir Probe Instrument: The Royal Institute of Technology in Stockholm operates a Langmuir Probe instrument, shown in Figure 2.6, on ROMEO to study the surrounding thermal plasma and its interaction with the satellite's water-based propulsion system. Two deployable probes mounted on the solar panels measure electron density, temperature, and plasma potential by applying a voltage to the probe

[4]Earthshine is sunlight reflected from Earth to the Moon's dark side and back, providing a way to measure Earth's albedo. Observing it from space improves accuracy compared to ground-based methods.

and measuring the electric current it collects. As the voltage changes, the probe either attracts electrons or ions from the plasma. When the voltage is very positive, the probe attracts a large number of electrons, and the current increases, eventually reaching electron saturation. This indicates the number of electrons in the plasma, its electron density. However, if the voltage is very negative, the probe repels electrons and attracts ions, reaching ion saturation. In between these two extremes, at the point where the current switches from being mostly ions to mostly electrons, the voltage is called the plasma potential. The shape of the curve (voltage-current) in this transition region gives the electron temperature, which tells how fast the electrons are moving.

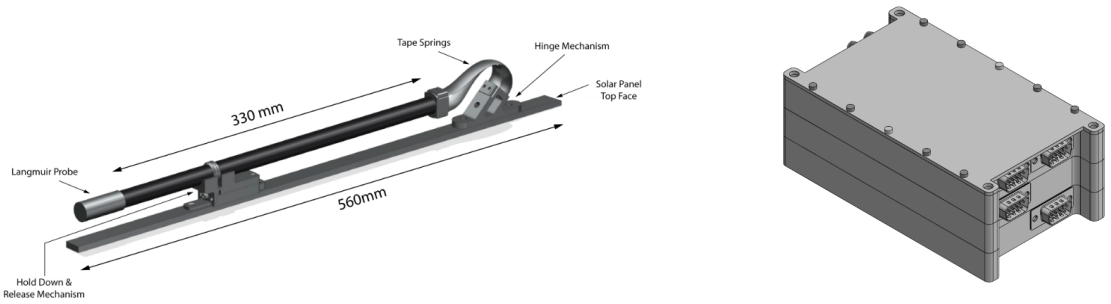

(a) Langmuir Probe in stowed configuration. (b) Langmuir Electronics.

Figure 2.6: Langmuir Probe Instrument.

Table 2.1 presents the operative temperature range of the Langmuir Instrument, which will serve as a reference to assess whether the results fall within acceptable limits.

Object	**Max Temperature** (°C)	**Min Temperature** (°C)
Langmuir probes	100	-50
Langmuir electronics	80	-40

Table 2.1: Operative Temperature of the Langmuir instrument.

2.5 Spacecraft Thermal Control

Thermal control is essential for maintaining the spacecraft's components within their specified temperature limits. It protects sensitive electronics, instruments, and structural elements from damage due to overheating or freezing. For the management of both external fluxes and internal heat, thermal control systems combine passive

and active elements. A general overview of spacecraft thermal control techniques is presented below to provide context. However, in the model used for this analysis, the ROMEO satellite implements only passive thermal control elements, such as Multi-Layer Insulation (MLI), radiating surfaces, and surface coatings with defined thermo-optical properties. No active thermal control systems were included in the simulation.

2.5.1 Passive Control

Passive thermal control relies on material properties and design to regulate heat without consuming power. These components are lightweight, reliable, and effective.

- **MLI**. MLI is often referred to as the spacecraft's "sleeping bag", and it consists of alternating layers of reflective Mylar film and low-conductance Dracon spacers, reducing radiative and conductive heat transfer. The outer surface involves a highly reflective Kapton film. MLI covers most of the spacecraft, with cut-outs for radiators and instruments.
- **Radiators**. Radiators are the primary means of rejecting excess heat into space. They are coated with high-emissivity materials to enhance heat radiation while maintaining low absorptivity to solar flux. They involve an adhesive film vapor-coated with a metal layer (e.g., aluminum or silver), which is covered by a transparent glass, quartz, or Teflon layer. Their placement and orientation are optimized to avoid direct sunlight and Earth's IR [5].
- **Surface Coatings and Finishes**. Surface treatments adapt emissivity and absorptivity properties to specific needs. For example, white paints reflect solar radiation, while black coatings maximize heat rejection. Polished aluminum or Optical Solar Reflectors (OSRs) are used where minimal heat absorption is desired.
- **Thermal Doublers and Heat Spreaders**. These components, often made of aluminum or advanced composites, distribute heat evenly across surfaces, reducing hotspots under high dissipation units like electronics.

[5]The transparent layer has very good properties in the infrared wavelength range (high ε), and efficiently dissipates the heat, but this means also Earth's IR absorption due to (2.17).

- **Heat Pipes**. Ammonia, methanol, or water in a closed vacuum tube uses capillary action to transport heat from the hot region to the radiators. They are sealed tubes containing a working fluid that evaporates at the heat source, travels as vapor to the cooler radiator, and condenses to release heat. This efficient, passive system operates without moving parts.
- **Interface materials**. Interface materials, such as Sigraflex graphite foil or Chotherm thermal fillers, improve the contact conductance between surfaces.
- **Heat sinks**. Heat sinks have high heat capacity and can lower the temperature of hot bodies, by attaching a piece of highly conductive material, like copper. In this way, the greater distribution of heat lowers the thermal density. A special heat sink, known as Phase-Change Materials (PCMs), consists of using the phase transition between solid and liquid to absorb heat during peak loads by melting and release it during cooler periods by solidifying.

2.5.2 Active Control

Active thermal control systems use power and dynamic regulation to manage temperatures more precisely, often complementing passive systems.

- **Heaters**. Heaters prevent components from dropping below their minimum temperature limits during cold phases, such as eclipses. These can include resistance wires embedded in Kapton tape or heaters mounted on specific hardware. They are controlled by software using thermistors for precise feedback.
- **Thermal Louvers**. Louvers regulate heat rejection by adjusting reflective panels to control radiator exposure. When closed, they reflect heat into the spacecraft, while opening allows maximum radiation.
- **Cooling Circulation System**. In high-power spacecraft, active cooling systems circulate a working fluid to remove heat from densely packed components. These systems include pumps and heat exchangers, offering precise thermal control.
- **Thermal Control Software**. Thermal software integrates with sensors and actuators to dynamically monitor and adjust the spacecraft's thermal state. This ensure optimal operation and reduces reliance on passive designs alone.

Chapter 3

Methodology

This chapter provides an overview of the research method employed in this thesis, outlining the workflow of the thermal analysis and the underlying assumptions. A fundamental understanding of the software environment and the previous work done on the ROMEO satellite is provided.

3.1 Model

The University of Stuttgart has provided a preliminary Systema-Thermica model of the entire satellite, which has been used in previous analyses. However, the model lacks a detailed representation of the Langmuir Probe instrument. The Langmuir probes and electronics are highlighted in purple in Figure 3.1. The Thermica applications globally transform the geometric model into a mathematical model and perform a complete thermal analysis of the space system orbiting around the Earth. On the thermal model, Thermica computes all the elements needed to simulate the temperature. The thermal solver, Thermisol, then performs the temperature computation [2].

To accurately model the Langmuir instrument, two separate models were developed: one for the Langmuir probes and another for the associated electronics. The components themselves were refined with greater detail, while the surrounding environment was simplified to reduce complexity and computational time. For the same reasons, each component has been represented with shell elements, which are 2D surface shapes.

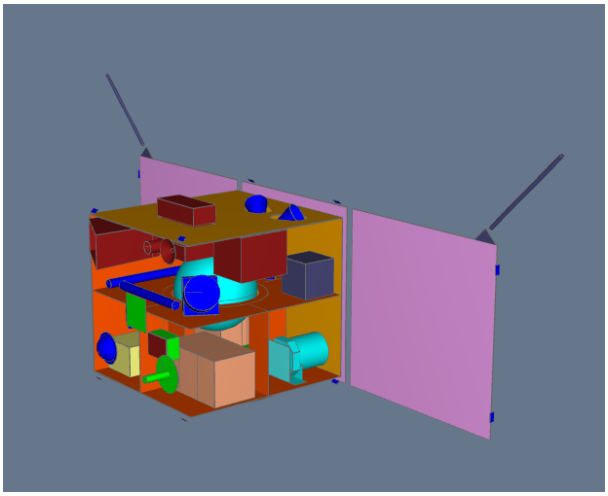

Figure 3.1: Preliminary model of the ROMEO satellite provided by the University of Stuttgart.

3.1.1 Langmuir Probes Model

The modeling approach for the Langmuir Probes was to include only the main outer structure (covered with MLI) and the solar panels, while removing all unnecessary components, as shown in Figure 3.2. The probes were modeled at the extremities of the booms, while the tape springs were represented through thermal couplings. Similarly, the connections between the solar panels, as well as between the solar panels and the satellite structure, were also implemented as thermal couplings. This modeling choice allows for an accurate representation of the thermal behavior of the system while significantly reducing complexity and computational cost.

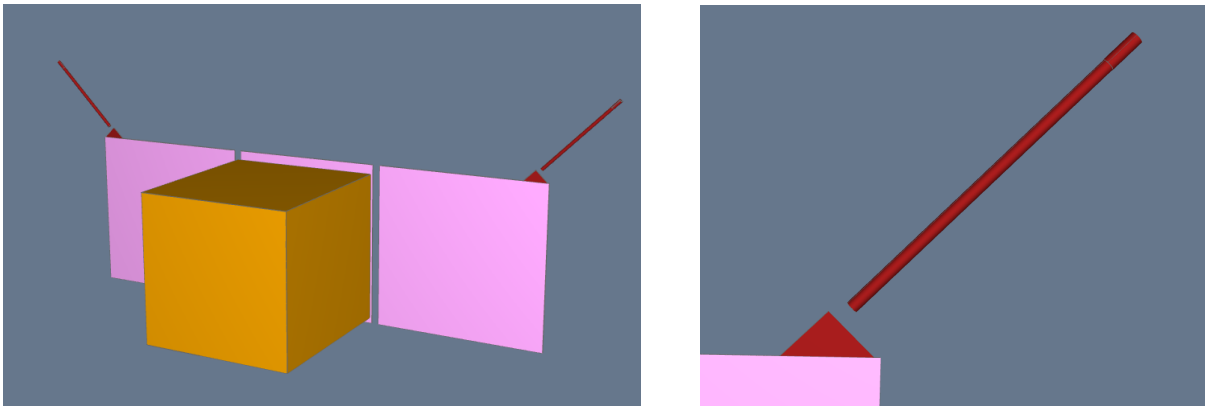

Figure 3.2: Langmuir Probes model.

The materials used in the model are listed in Table 3.1. The mass of the MLI and the material selection for the solar panel are still undefined.

Object	**Material**	**Mass** (kg)
Langmuir Probe	Aluminium (Al)6061	0.008
Hinge Mechanism	Al6061	0.045
Boom	CFRP	0.035
Tape Spring	Stainless Steel (SS)316	0.005
Solar panel right	Sandwich structure	2.572
Solar panel left	Sandwich structure	2.572
Solar panel body	Sandwich structure	1.377
Side Plate Left	CFRP [0/60/-60]s - Honeycomb Structure – CFRP [0/60/-60]s	1.458
Side Plate Right	CFRP [0/60/-60]s - Honeycomb Structure – CFRP [0/60/-60]s	1.458
Front Plate	CFRP [0/60/-60]s - Honeycomb Structure – CFRP [0/60/-60]s	1.458
Service Plate	CFRP [0/60/-60]s - Honeycomb Structure – CFRP [0/60/-60]s	1.476
Payload Plate	CFRP [0/60/-60]s - Honeycomb Structure – CFRP [0/60/-60]s	1.267
Core Module	CFRP [0/60/-60]s - Honeycomb Structure – CFRP [0/60/-60]s	1.045
Core Shear Plate (1,2,3,4)	CFRP [0/60/-60]s - Honeycomb Structure – CFRP [0/60/-60]s	0.103
MLI	MLI	-

Table 3.1: Materials.

The properties of each object were also defined: the bulk properties are listed in Table 3.2, while the coating properties are shown in Table 3.4.

	Geometrical Properties	**Physical Properties**		
Object	**Thickness** (m)	**Conductivity** (W/K/m)	**Specific heat** (J/K/kg)	**Density** (kg/m^3)
Langmuir Probe	0.01	170	900	8028.949
Hinge Mechanism	0.01	170	900	8028.949
Boom	0.01	18	935	1540
Solar panel	0.015	4.98	481.676	659.641
Payload Plate	0.018	8.8579	2780	348.611
Service Plate	0.018	8.8579	2780	355.931
Side Plate Left	0.018	8.8579	2780	354.907
Side Plate Right	0.018	8.8579	2780	354.907
Core Shear Plate	0.018	8.8579	2780	326.359
Core Shear Plate (1)	0.018	8.8579	2780	296.690
Core Shear Plate (2)	0.018	8.8579	2780	296.690
Core Shear Plate (3)	0.018	8.8579	2780	315.831
Core Module	0.018	8.8579	2780	348.611
Front Plate	0.018	8.8579	2780	412.385
MLI	0.005	0.07	1783.3	379.5

Table 3.2: Bulk properties [10].

In the thermal model, the density assigned to each structural plate was locally adjusted, as detailed in Table 3.2, to ensure that the satellite's total mass matches the actual reference value. In Thermica, density is used not only to calculate the spacecraft's total mass but also to determine the thermal capacity of each component. Therefore, assigning consistent and physically meaningful density values is essential for achieving accurate and reliable thermal simulations.

The transverse conductivity, shown in Table 3.3, refers to the thermal conductivity perpendicular to the main surface, across the thickness of the layer. It is especially relevant when modeling anisotropic materials, whose thermal properties differ depending on the direction, typical of layered structures like solar panels. For some elements, it is neglected because it is not relevant.

Object	**Transverse conductivity** $(\mathrm{W} \cdot \mathrm{K}^{-1} \cdot \mathrm{m}^{-2})$
Solar panel right and left	134.683
Side plate right and left of the structure	92.758
MLI	14

Table 3.3: Transverse properties.

Table 3.4 shows that the service plate of the structure has distinct optical properties, as it is not covered with MLI but with Fluorinated Ethylene Propylene (FEP), a second-surface mirror coating characterized by low absorptance [8].

Object	**Thermo-optical IR** ε	**Thermo-optical UV** α
Langmuir Probe	0.56	0.44
Hinge Mechanism	0.56	0.44
Boom	0.9	0.95
Solar panel	0.85	0.91
Payload and side plates	0.85	0.93
Service plate	0.726	0.068
MLI	0.64	0.39

Table 3.4: Coating properties.

3.1.2 Langmuir Electronics Model

The modeling approach for the Langmuir Electronics was to include only the main outer structure (covered with MLI), the internal structure, and the tank, while removing all unnecessary components as shown in Figure 3.3. The blue sphere in the middle represents the tank, while the electronics box (in red) location was updated to better accommodate the allocation of other components. The Langmuir Electronics consists of a top lid and three separate boxes: the power box, system A box, and system B box, as shown in Figure 2.6b. However, since all components are made of the same material and are in good thermal contact, the entire assembly has been modeled as a single unified box. To validate this approach, boundary conditions such as the

temperature of the MLI and the surrounding plates of the electronic box were taken into account.

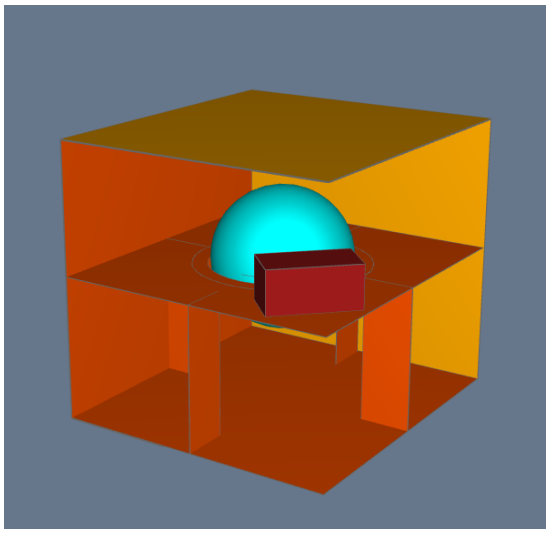

Figure 3.3: Langmuir Electronics model.

The internal structure presents the same properties as the outer one, used in the Langmuir Probes model, as shown in Table 3.2. The materials of the tank and the Langmuir Electronics can be observed in Table 3.5.

Object	**Material**	**Mass** (kg)
Langmuir Electronics	Al6061	0.7
Tank without water	Al with MLI	1.155
Tank with water	Al with MLI	13.155

Table 3.5: Materials of the tank and Langmuir Electronics.

The bulk properties of the tank and Langmuir Electronics were also defined and are shown in Table 3.6. The density assigned to the tank is notably high, as it accounts for the presence of water inside, since the fluid itself is not explicitly modeled. On the core module, there is a circular object around the tank which has no bulk properties (except 0.001 m thickness), which is likely a non-physical surface, introduced in the model to enable or control radiative heat exchange between the tank and its surroundings. It does not represent an actual structural part, but rather serves as a geometric and thermal reference surface within the simulation. The tank also presents a transverse conductivity of 113333 $W \cdot K^{-1} \cdot m^{-2}$, which is quite high due to its thin wall thickness.

	Geometrical Properties	**Physical Properties**		
Object	**Thickness** (m)	**Conductivity** (W/K/m)	**Specific heat** (J/K/kg)	**Density** (kg/m^3)
Langmuir Electronics	0.002	170	900	2500
Tank	0.0015	170	900	84862

Table 3.6: Bulk Properties of the tank and Langmuir Electronics.

The thermo-optical properties are listed in Table 3.7. It can be observed that the tank coating properties vary between its inner and outer surfaces: the interior is bare aluminum, while the exterior is coated with a gold-like material to enhance its thermal performance.

Object	**Thermo-optical IR** ε	**Thermo-optical UV** α
Langmuir Electronics	0.56	0.44
Tank positive side	0.05	0.3
Tank negative side	0.56	0.44

Table 3.7: Coating properties.

3.2 Meshing

Meshing is used to perform the analysis by generating identifiable nodes through the division of the model's geometrical shapes into smaller parts (meshes). This process allows the preparation of the elements on which the thermal computations are performed, such as conduction paths and radiative exchanges. The software can automatically compute the radiative couplings (GR) and the conductive couplings (GL) when no cut-outs are present and the contact between nodes is properly defined, such as for nodes belonging to the same surface. When this is not the case, the conductive couplings must be computed manually and defined through a user file, a text file that allows the user to override or customize specific simulation inputs.

By default, Thermica creates a $SpaceNode$ among the non-geometrical nodes. This node represents deep space, at a very low temperature, typically around 2.7 K. Initially, the $SpaceNode$ is not connected to any geometrical surfaces. However, radiative couplings towards the Space Node are automatically established during the view factor calculation, ensuring that surfaces exposed to space are correctly linked in the thermal network and can radiate heat away.

3.2.1 Langmuir Probes Mesh

The model has been meshed, as shown in Figure 3.4. The solar panels, the structure, and the MLI feature both a positive-side and a negative-side mesh, allowing the distinction between thermal behavior on either side of each surface. Instead, each element of the Langmuir Probe has been meshed as a single node.

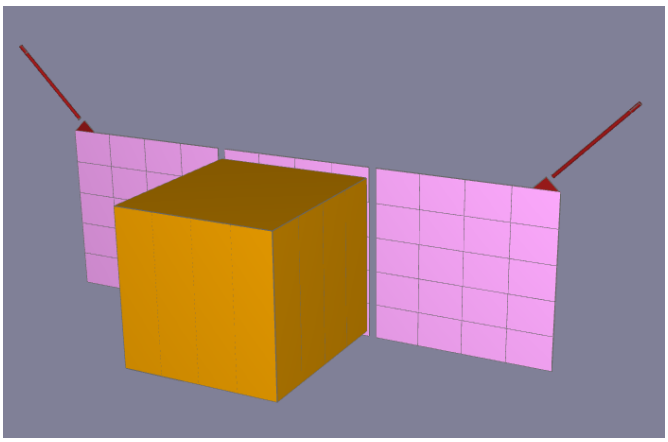

Figure 3.4: Langmuir Probes mesh.

3.2.2 Langmuir Electronics Mesh

The model has been meshed, as shown in Figure 3.5. The tank, the structure, and the MLI feature both a positive-side and a negative-side mesh, allowing the distinction between thermal behavior on either side of each surface. The circular object on the core module surrounding the tank was meshed without distinguishing between positive and negative sides. The electronics box, on the other hand, was meshed, taking into account that it is not a single component in reality, but rather composed of three separate boxes.

In this model, the tank was located in a cut-out in the core module, resulting in a geometric separation between the tank and the surrounding structure. However, when cut-outs are applied in Thermica, the software does not automatically compute thermal couplings across the edges. This is because the cut surfaces are treated as disconnected and without explicitly defined contact, so Thermica cannot assume physical continuity. To address this, an auxiliary mesh was introduced to help ensure correct computation of thermal couplings and view factors by recreating the thermal context lost due to the presence of the cut-out. This auxiliary mesh replicates the original features, except for the core module, where the cut-out was applied, which was not meshed

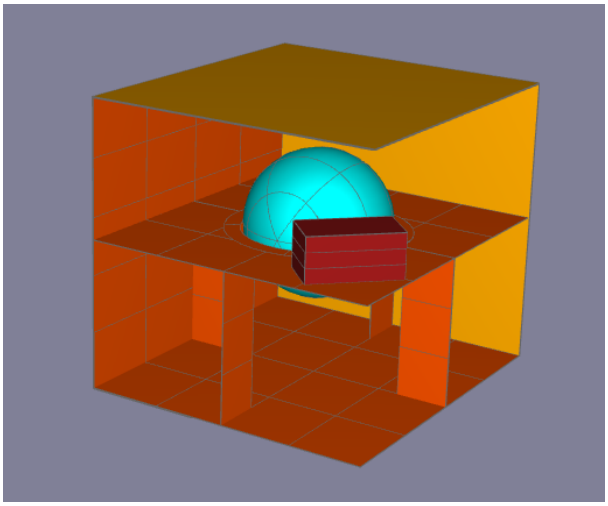

Figure 3.5: Langmuir Electronics mesh.

and therefore excluded from the thermal processing. Further details are provided in Section 3.4.

A total power dissipation of 5 W was considered for the electronics box in the hot case scenario. This dissipation was uniformly distributed among the associated nodes to ensure a consistent thermal input across the component.

Furthermore, the boundary conditions listed in Table 3.8 have been applied as fixed temperatures to the plates surrounding the box and to the MLI, due to the simplification of the model. These temperature values are based on the analysis conducted by the University of Stuttgart on the complete satellite model, which takes into account the power dissipation of the individual components. Compared to the values reported in Table 3.8, the original analysis indicated temperatures higher by +10°C for the cold case and lower by -10°C for the hot case. These adjustments were made to ensure a conservative approach and to account for uncertainties in the thermal environment.

Object	Hot Case	Cold Case
Structure	29°C	-18°C
MLI	70°C	-32°C

Table 3.8: Boundary condition for Langmuir Electronics.

3.3 Kinematics and Trajectory

The thermal analysis has been divided into two distinct cases, representing the worst-case scenarios for the ROMEO satellite: the hot case and the cold case. Both scenarios have been identified for conditions occurring in MEO orbit, where the revolution around the Earth requires 1 h 53 min 55 s. The reference date is set to the Spring Equinox, which marks the beginning of the orbit definition in this analysis. The orbital parameters can be observed in Figure 3.6 and are listed in Table 3.9, where the orbit of reference is the Earth.

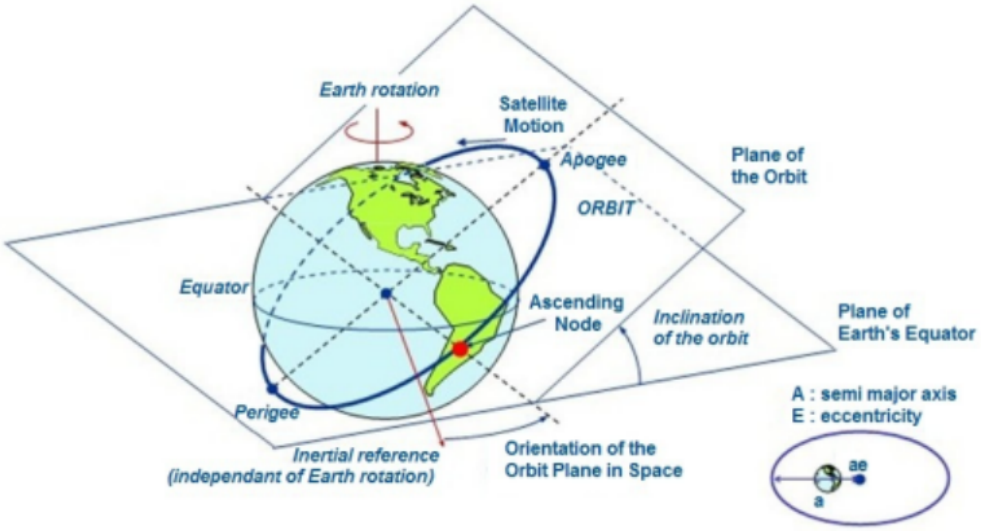

Figure 3.6: Orbital geometry and key parameters defining a satellite's orbit around Earth [1].

Parameter	Hot Case	Cold Case
Periapsis (km)	6700	6700
Apoapsis (km)	8870	8870
Inclination (°)	97.6	97.6
Argument of periapsis (°)	180	0
Local Time of Ascending Node (LTAN)	06:00:00 (True Solar Time (TST))	12:00:00 (Mean Solar Time (MST))

Table 3.9: Orbital parameters.

3.3.1 Hot case

In this scenario, the mode identified is the Idle, with the solar panels always pointing towards the Sun. The idle mode is an operational state in which active attitude determination is maintained, and Science and Electrolysis (during the transfer phase)

can be active as optional subsystems. The periapsis and the apoapsis define the ellipse. The ascending node occurs at 06:00:00 TST, meaning the satellite will cross the equator heading north at that local solar time, and the argument of the periapsis is 180°. These parameters represent the hot worst-case thermal conditions, maximizing the solar exposure.

3.3.2 Cold Case

In this scenario, the mode identified is the Safe Data-dowlink with S-band (DDS), with minimal components on. Here, the argument of the periapsis is zero, and the ascending node occurs at 12:00:00 MST. These parameters represent the cold worst-case thermal conditions, minimizing illumination. At the beginning of the orbit, the satellite is in eclipse until 19 min 27 s, and exits the penumbra at 19 min 41 s. Toward the end of the orbit, it enters the penumbra 19 min 44 s before the end of the orbit, and transitions into the umbra at 19 min 31 s before the end.

3.4 Processing

A processing diagram defines a sequence of processes specified for the associated application. Each basic process generally consists of input files, a description of the process itself, and output files. For this analysis, the mission configuration, which includes the geometrical model, trajectory, and kinematic model, is provided as input, considering the EOL phase for the hot case and the BOL phase for the cold case. This setup enables the simulation of the satellite's geometric movement within the specified simulation environment. By default, the mission process generates two files: the mission set file (.sysset), used by other applications, and the mission data file (.html), which can be consulted by the user and disabled if not required. The Thermica application is organized into modules based on sub-applications, each managing specific Thermica entities [2]. Every module defines its own input files, parameters, and output files. A solar constant of 1428 W/m² for the hot case and 1316 W/m² for the cold case has been considered as a common run parameter.

3.4.1 Nodal description

This module is used to translate the nodal breakdown, including the geometrical mesh and specific elements. It is affected by the bulk, transverse, and coating properties. In a nodal thermal model, nodes represent the unknowns for which the temperature will be calculated. Each node is an element of the model that carries specific physical properties and is connected to its surrounding environment through thermal couplings. A node can represent a single shape, a group of shapes, or a portion (mesh) of a shape, and it is assumed to be isothermal, meaning that a single, average temperature is computed for its entire geometrical representation.

3.4.2 Conduction

This module is used to create conductive links between meshes. These links are created through edge nodes that are also generated by this module. When computing radiative couplings or external fluxes, surface nodes are assumed to be isothermal, which means each surface has a uniform temperature. However, conduction requires a temperature gradient, which cannot be represented if we assume surfaces are completely isothermal. To overcome this, Thermica introduces interface nodes, known as edge nodes. These nodes represent the average temperatures along free edges or at contact points, allowing the model to capture temperature variations within a surface. In addition, the surface node itself is redefined to represent the average temperature of the entire surface, rather than just its central point.

The conductive heat exchange between nodes is governed by Fourier's law (2.1), which, applied to the nodal network, allows the computation of conductive power transfers. To perform this efficiently, Reduced Conductive Network (RCN) method is employed. The conductive network is built starting with the introduction of edge nodes. Surface nodes are also taken into account to accurately represent heat conduction through the geometry. The computation is based on a detailed sub-mesh of each node, which allows for a more refined analysis of the internal conductive paths. From this sub-mesh, elementary conductive couplings between adjacent elements are calculated. These couplings are then assembled into a full conductive network, representing the overall conductive behavior of the system. Finally, this detailed network is reduced to a simplified form, preserving the essential thermal characteristics while optimizing the computational efficiency. A simplified RCN method is derived from the original RCN

approach to provide shape-to-shape conductive couplings. In this case, the conductive flux is approximated by assuming a piecewise linear temperature profile perpendicular to each edge. Thermica first computes the full RCN solution for each node and then simplifies it by assuming a linear flux normal to one edge.

One of the main limitations of the conduction module lies in the fact that its algorithm does not account for Boolean transformations, such as the use of cut-outs (i.e., subtractive geometric operations), in the computation of conductive couplings. As a result, any shape that has been modified through Boolean operations is excluded from the conductive network, and no conductive heat transfer is computed through that geometry. This constraint may lead to inaccuracies in thermal analysis. To overcome this, conductive coupling can be computed manually according to Equation (2.8) and inserted in the meshing tab, or in the user file, as explained in Section 3.4.6. The Langmuir Probes model does not have cut-outs, so the conductive module has been used without any issues. Instead, the Langmuir Electronics model includes a cut-out on the core module to accommodate the tank. Therefore, a different modeling approach was required to ensure an accurate thermal analysis, avoiding errors. To compute the conductive couplings needed for the simulation, two distinct processes were carried out. The first involved a preliminary simulation in which the core module was intentionally excluded from the mesh, as described in Section 3.2.2. This configuration enabled the extraction of all necessary information on edge nodes and conductive couplings using the RCN method. The resulting data were taken from the gl.nwk output file generated by the conduction module. The second simulation constituted the actual thermal analysis. In this case, the previously extracted coupling and edge data were manually incorporated into the user input file. Moreover, since the core module was not included in the first simulation, the conductive couplings involving the core module and the tank were manually calculated and added to the same user file to complete the model.

3.4.3 Radiation

This module is used to create radiative links. It computes the thermal radiative couplings between the geometrical nodes of a model, and it is impacted by the Monte-Carlo Ray tracing method. Additionally, it exports radiative exchange factors to a discretized surrounding box that represents the various directions of space. This

output is essential for the Planet fluxes module and can also be used to accelerate the computation of Solar fluxes. The box file contains not only the direct view factors to space, but also radiative exchange factors in both the IR and visible spectral ranges. When enabled, the Radiation module performs calculations in both spectra to provide the corresponding data within the box file.

3.4.4 Solar flux

This module is used to give the quantity of solar flux collected by each mesh. To compute the flux, it is necessary to define both the orbit and the spacecraft's pointing. The calculation is carried out at multiple positions along the orbit. At each point, the spacecraft's position and orientation are automatically determined, as well as the positions of the planet and the Sun. The process begins by randomly distributing several points over each node. For each point, the algorithm checks whether it is oriented towards the Sun. Once this is established, ray tracing is used to determine whether the point is in shadow. If the point is both facing the Sun and not occulted, it is considered directly illuminated, and the corresponding ray energy is transferred to the node. After this, the ray is re-emitted from the point to account for contributions from extended sources and ambient radiation.

3.4.5 Planet flux

This module is used to give the quantity of planet albedo and IR fluxes collected by each mesh. The computation of IR and albedo fluxes involves a series of preliminary steps that integrate with the REF calculation. During the REF computation, rays that escape into space are tracked and collected. A virtual sphere, placed at an infinite distance, is used to capture the direction of these escaping rays. This sphere is divided into mesh elements, and view factors are calculated between each surface of the satellite and each element of the sphere. To determine the contribution from the planet, the mesh of this virtual sphere is then projected radially onto the planet's surface. For each projected element, the algorithm evaluates whether it falls on the day or night side of the planet, allowing it to compute the proportion of light received. The algorithm adds a specific processing step dedicated to calculating the planet's IR and albedo contributions. It does this by introducing a unit box centered on the spacecraft and virtually located at infinity, treating the spacecraft as a point source. This box is uniformly meshed,

and during the ray-tracing process, rays that do not hit any part of the satellite are instead assigned to a specific element of the unit box. The energy carried by each of these rays is accumulated in the corresponding element of the box. By the end of the ray-tracing phase, in addition to the internal thermal couplings between nodes, the algorithm has also determined the radiative couplings between the spacecraft and the surrounding space data, which are essential for computing both planetary albedo and IR fluxes.

In particular, the Earth's properties used in this module have been defined according to the specific thermal scenario under analysis, as reported in Table 3.10.

Properties	Hot Case	Cold Case
Earth Temperature	-13.15°C	-29.15°C
Earth Albedo	0.41	0.19

Table 3.10: Earth's properties.

3.4.6 Temperature Solver

The temperature solver is the main module of Thermisol, based on the ESATAN language [3]. The input data are defined through one or more text files, using a Fortran-like syntax to describe the nodal network as well as any time or temperature-dependent behaviors. This structured input is then automatically translated into Fortran code, which is subsequently compiled and linked with a dedicated computational library. The result is an executable program that performs the numerical simulation and outputs the thermal solution of the system. The interface between Thermisol and Thermica is given by the Skeleton module. The purpose is to collect the network files coming from Thermica and to include them in a standard skeleton of the input file dedicated to Thermisol temperature solver.

In this work, a user input file was provided to support the Thermisol temperature solver. This custom text file (.txt) allows the user to manually define or override thermal couplings, edge connections, and node properties that are not automatically generated by the software.

For the Langmuir Probes simulation, the conductive couplings (GL) representing the connections between the solar panels and between the solar panels and the main structure were derived from the previous analysis conducted by the University of Stuttgart and directly inserted. The conductive links representing the tape spring

connection between the boom and the hinge mechanism were manually calculated according to Equation (2.8), as were those between the boom and the probe.

In the Langmuir Electronics simulation, the GL couplings between the core module nodes, as well as those connecting the tank to the core module, were also provided by Stuttgart's previous study. The couplings between the electronics box and the core module were manually computed using the same approach described in Equation (2.8), and included in the user file.

Finally, the user file also includes the definition of internal power dissipation. In particular, the 5 W dissipation was specified for the electronics box in the hot-case scenario.

When dealing with complex geometries, large Excel files are employed to perform all the necessary calculations for thermal couplings. For each pair of nodes, parameters such as the contact area, thermal conductivity, conductive length, contact resistance, and heat transfer coefficient are given. Using these values, the Excel workbook computes the conductive coupling according to Equation (2.8).

To automate the formatting and export of the results, Excel macros are used. These macros are small scripts written in Visual Basic for Applications (VBA) that allow repetitive tasks to be executed automatically. In this case, the macro collects the calculated data from the spreadsheet and organizes it into a user file formatted according to the requirements of Thermica (.txt). This process significantly reduces manual work, ensures consistent formatting, and improves overall efficiency.

Furthermore, the simulation was configured with the stabilized cycle time option, which allows Thermica to simulate several orbital periods until a thermally periodic steady state is achieved. The tool automatically stops the simulation once the temperature difference between consecutive cycles becomes negligible, thus optimizing computational effort while preserving accuracy.

Chapter 4

Results

This chapter presents the results of the thermal simulations carried out using Systema-Thermica with the stabilized cycle time option. The analysis focuses on worst-case scenarios to assess the overall thermal behaviour and evaluate the performance of the Langmuir Probe instrument. Temperature, solar, and planet fluxes are provided.

4.1 Langmuir Probes Results

Taking the direction pointing toward the Earth as the reference ”right” side, Table 4.1 helps to interpret the graphs by indicating which nodes correspond to which part of the instrument they represent. The bottom surface of the cylindrical boom is referred to as the interactive disc bottom, while the top surface of the cylindrical probe is referred to as the interactive disc top.

Element	Node
Left boom	10500
Right boom	10600
Left Hinge	10700
Right Hinge	10800
Interactive disc right bottom	10900
Interactive disc left bottom	11400
Probe left	11000
Probe right	11100
Interactive disc left top	11200
Interactive disc right top	11300

Table 4.1: Correspondence between Langmuir probe elements and simulation nodes.

4.1.1 Hot Case

In the hot case scenario, the temperature distribution is shown in Figure 4.1. The time dependence of temperature for the booms is presented in Figure 4.2, while the results for the hinge mechanism are reported in Figure 4.3. Due to the solid mechanical connection, nodes 11000 and 11200 follow the same time dependence of temperature as node 10500, while nodes 11100 and 11300 follow the time dependence of temperature of node 10600. For good readability, they have not been plotted.

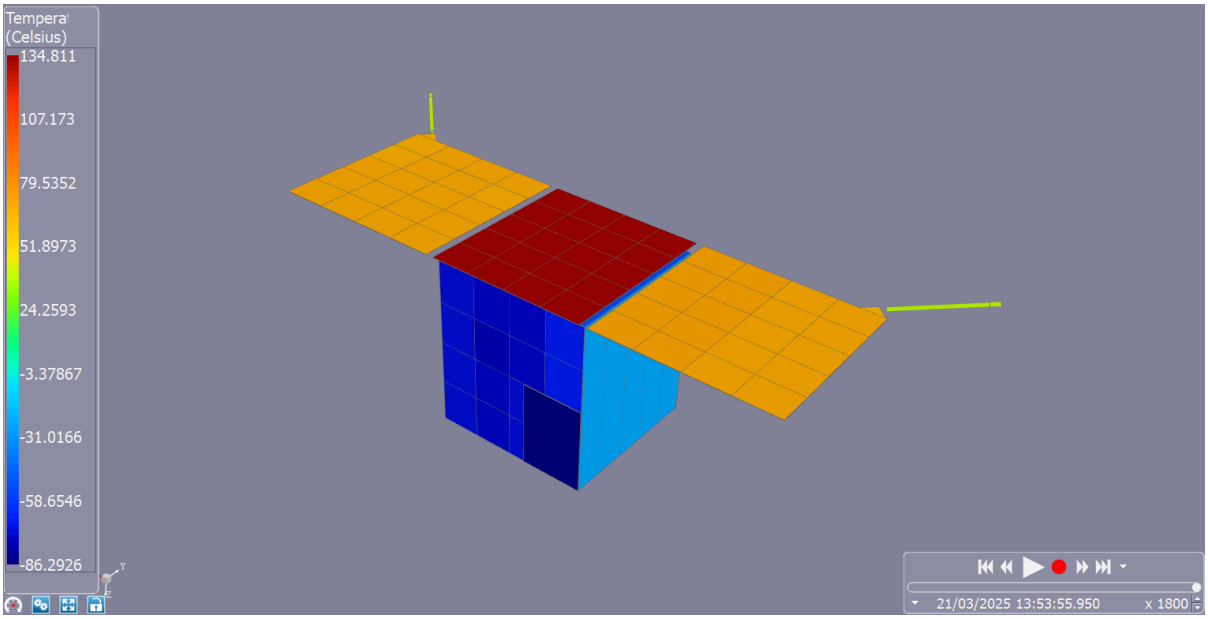

Figure 4.1: Temperature distribution of the Langmuir Probes at the end of the simulation time in the hot case scenario.

The maximum temperature reached by each node is reported in Table 4.2, showing that the operational range, shown in Table 2.1, is respected.

The time dependence of the absorbed solar flux, which takes into account the direct solar flux and the properties defined for each object, can be observed in Figure 4.4 and Figure 4.5. All the nodes exhibit little variation over time, except for the interactive disc, which likely undergoes phases of penumbra.

The time dependence of the absorbed albedo flux, which takes into account the direct albedo flux and the properties defined for each object, can be observed in Figure 4.6 and Figure 4.7.

The time dependence of the absorbed IR flux, which takes into account the direct infrared flux and the properties defined for each object, can be observed in Figure 4.8

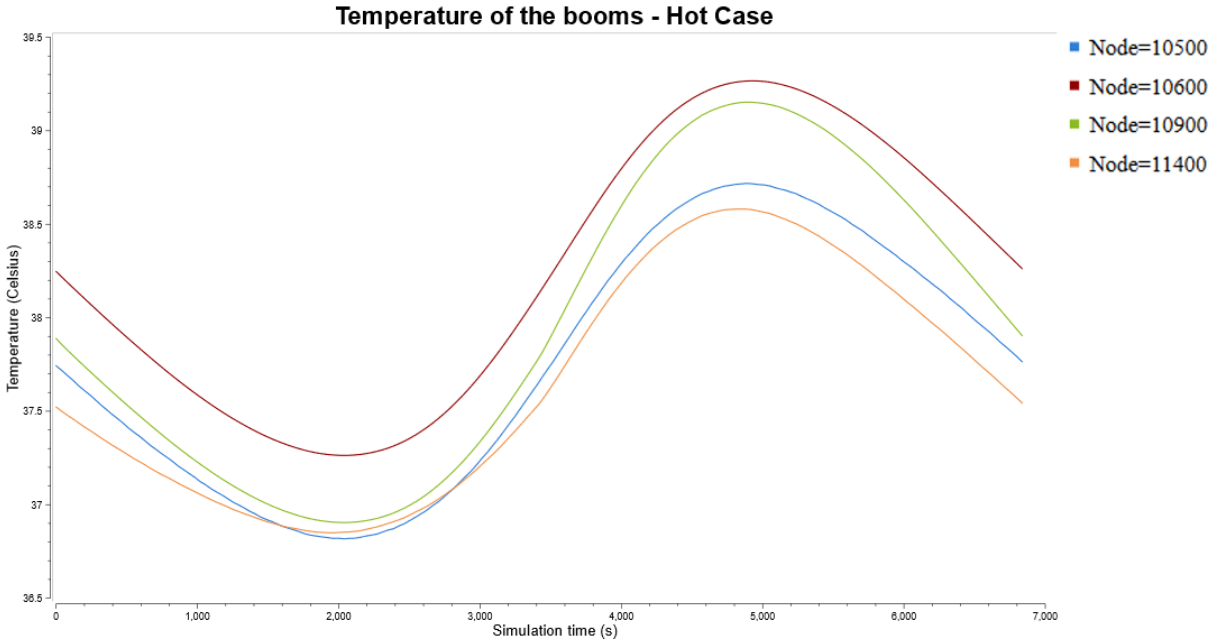

Figure 4.2: Time dependence of temperature of the booms when an equilibrium is reached in the hot case scenario. Table 4.1 provides a reference for the correspondence between shapes and nodes.

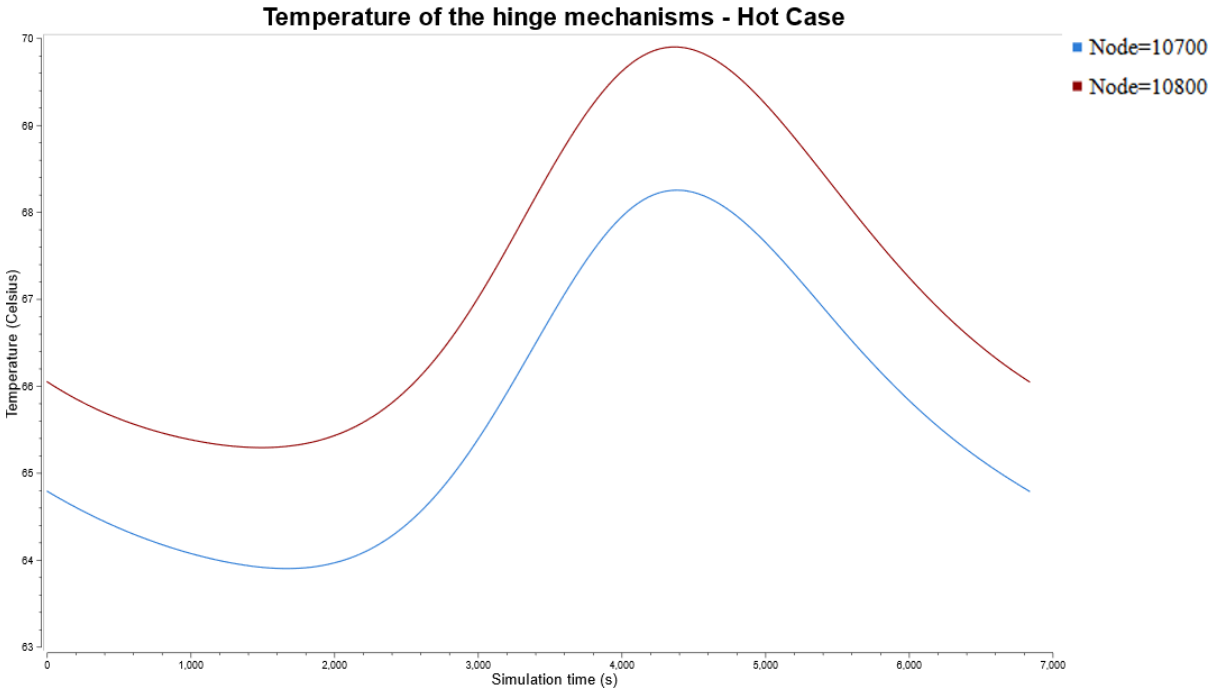

Figure 4.3: Time dependence of temperature of the hinge mechanisms when an equilibrium is reached in the hot case scenario. Table 4.1 provides a reference for the correspondence between shapes and nodes.

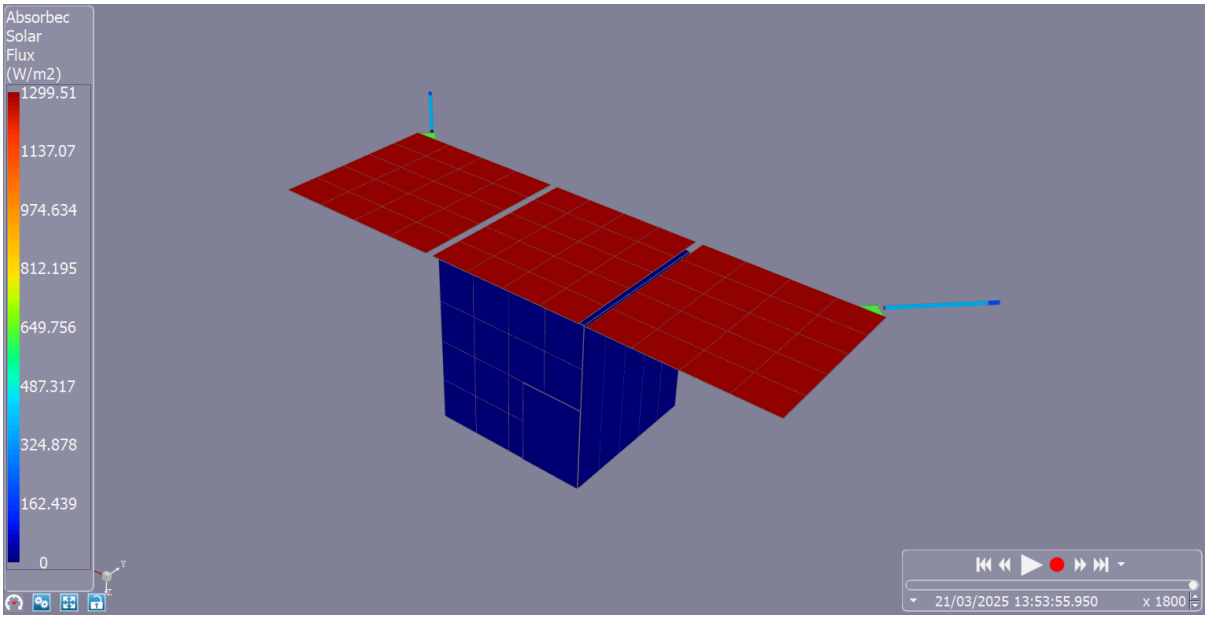

Figure 4.4: Solar absorbed flux on the Langmuir Probes model at the end of the simulation time in the hot case scenario.

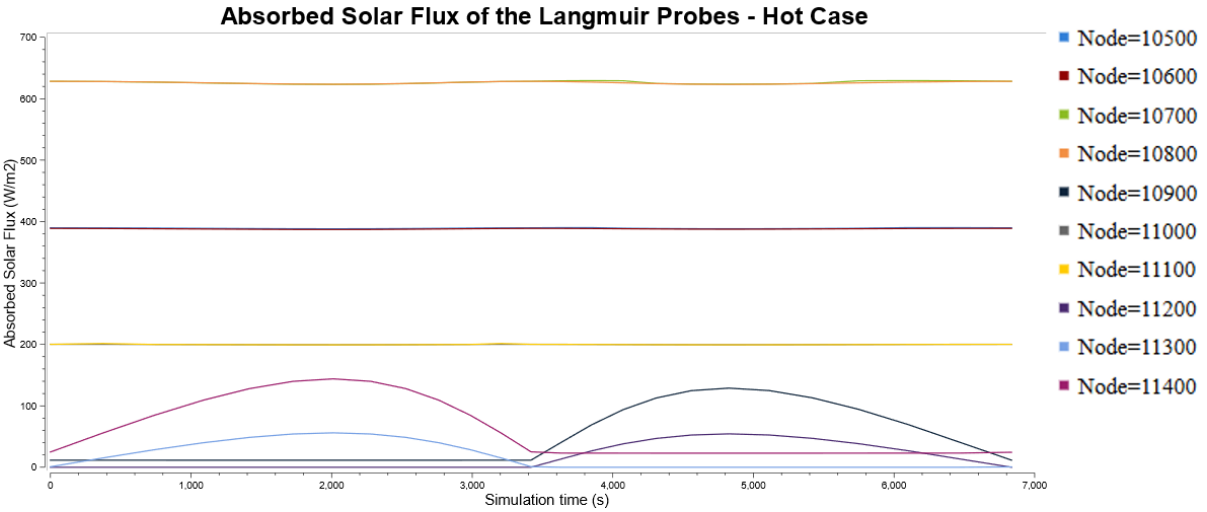

Figure 4.5: Time dependence of the solar absorbed flux of the Langmuir Probes in the hot case scenario. Table 4.1 provides a reference for the correspondence between shapes and nodes. Nodes 10500 and 10600 exhibit the same time dependence of temperature, as do nodes 10700 and 10800, and nodes 10000 and 11000.

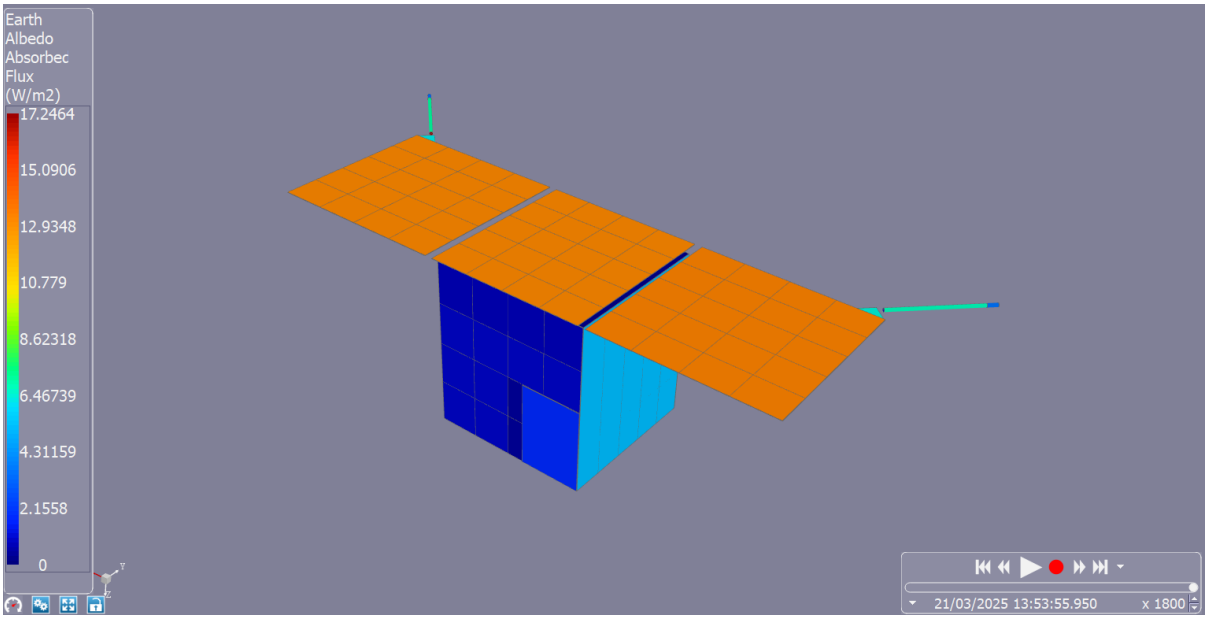

Figure 4.6: Albedo absorbed flux on the Langmuir Probes model at the end of the simulation time in the hot case scenario.

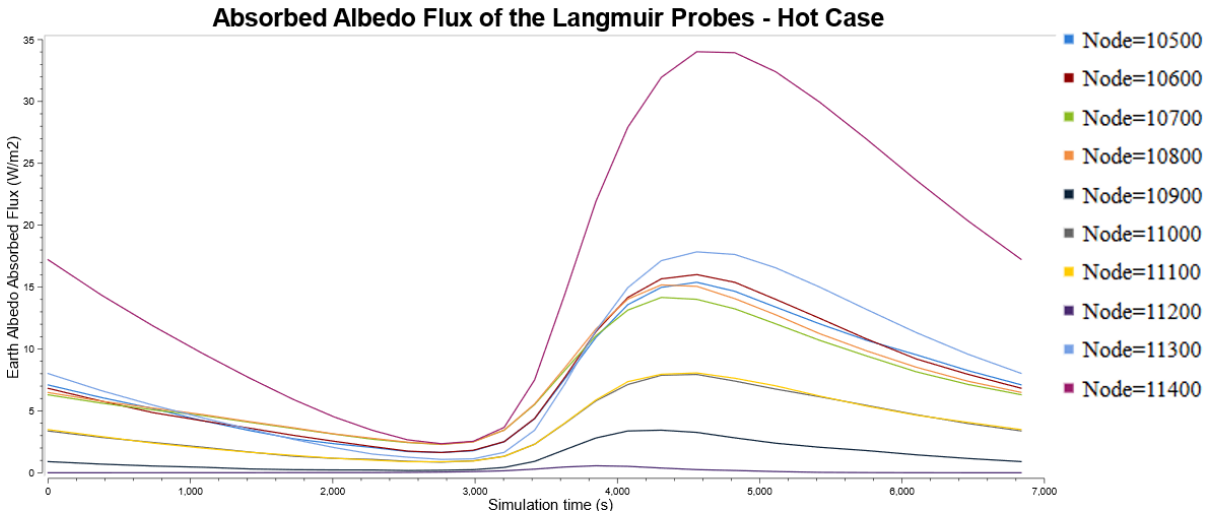

Figure 4.7: Time dependence of the albedo absorbed flux of the Langmuir Probes in the hot case scenario. Table 4.1 provides a reference for the correspondence between shapes and nodes.

Element	Node	Max Temperature (°C)
Left boom	10500	38.7
Right boom	10600	39.3
Left Hinge	10700	68.3
Right Hinge	10800	69.9
Interactive disc right bottom	10900	39.2
Interactive disc left bottom	11400	38.6
Probe left	11000	38.7
Probe right	11100	39.3
Interactive disc left top	11200	38.7
Interactive disc right top	11300	39.3

Table 4.2: Maximum temperature reached by each node of the Langmuir Probes during the hot case.

and Figure 4.9. The elliptical shape of the orbit is clearly observable, starting from the farthest point from Earth, passing through the closest point at mid-orbit where the IR is higher (the peak), and then returning to the initial position.

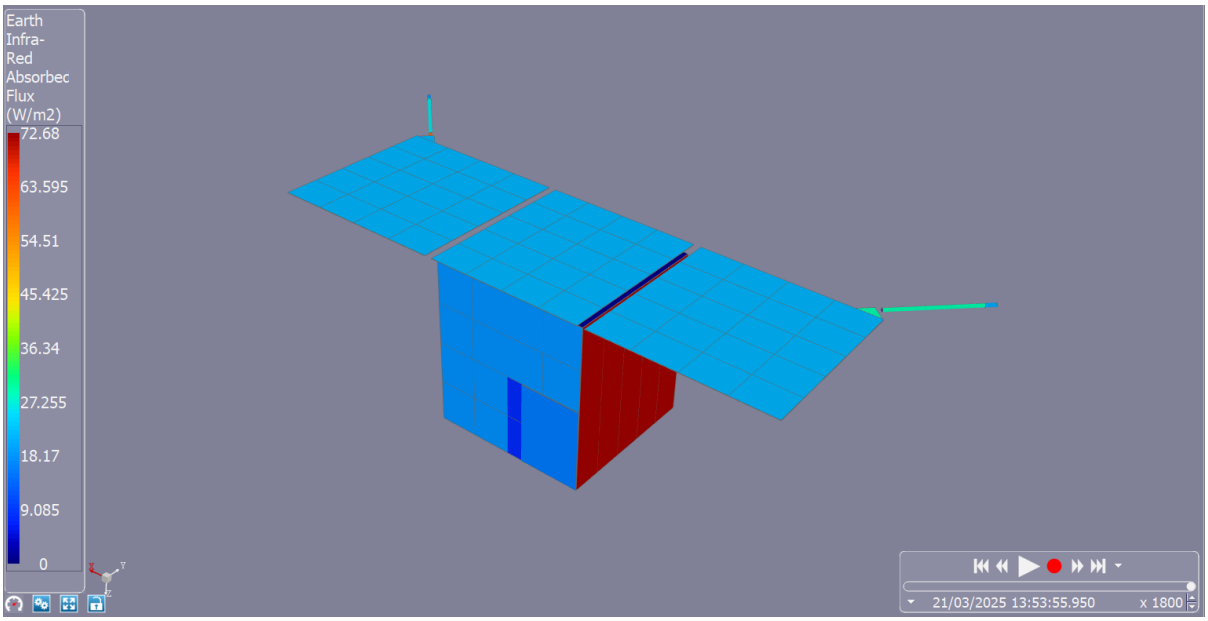

Figure 4.8: IR absorbed flux on the Langmuir Probes model at the end of the simulation time in the hot case scenario.

4.1.2 Cold Case

In the cold case scenario, the temperature distribution is shown in Figure 4.10. The time dependence of temperature for the booms is presented in Figure 4.11, while the results for the hinge mechanism are reported in Figure 4.12. Due to the solid mechanical connection, the probes likely follow the same time dependence of

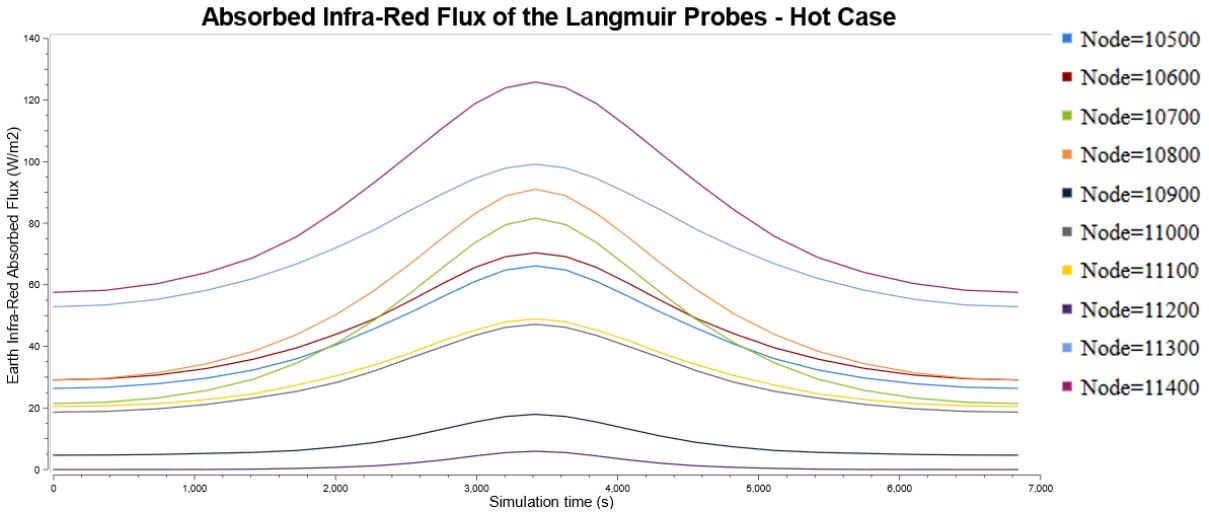

Figure 4.9: Time dependence of the IR absorbed flux of the Langmuir Probes in the hot case scenario. Table 4.1 provides a reference for the correspondence between shapes and nodes.

temperature as the booms. For clarity, nodes 11000, 11100, 11200, and 11300 are not plotted, as nodes 11000 and 11100 show the same time dependence of temperature as node 10500, while nodes 11200 and 11300 follow the same behavior as node 10600.

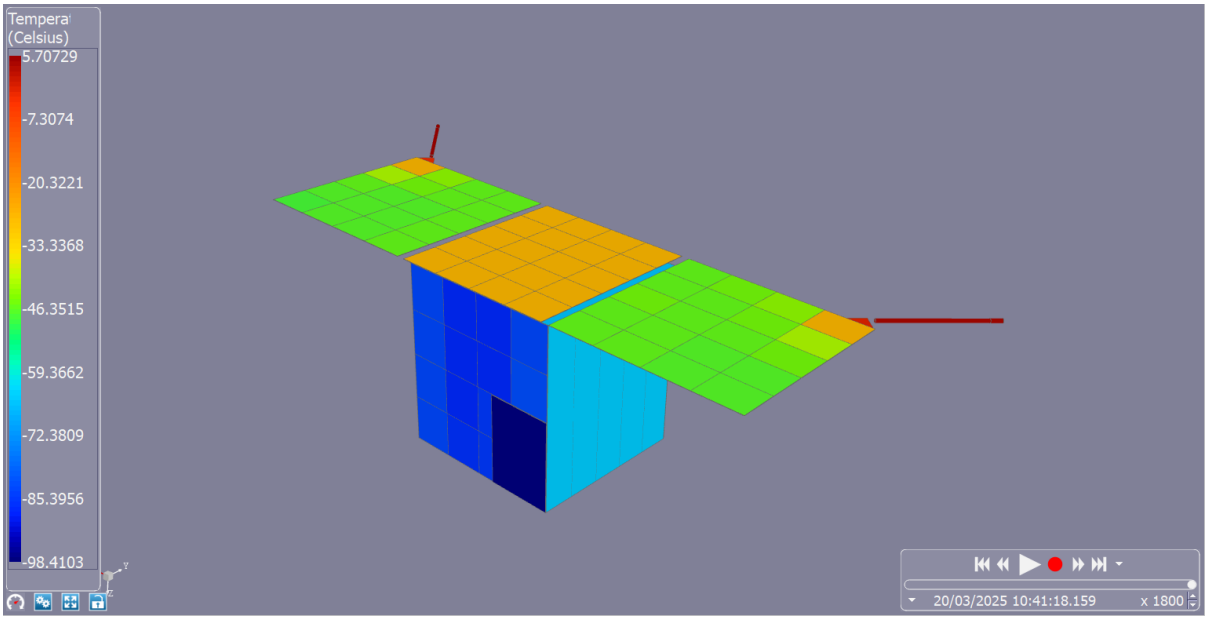

Figure 4.10: Temperature distribution of the Langmuir Probes at the end of the simulation time in the cold case scenario.

The minimum temperature reached by each node is reported in Table 4.3, showing that the operational range, shown in Table 2.1, is respected.

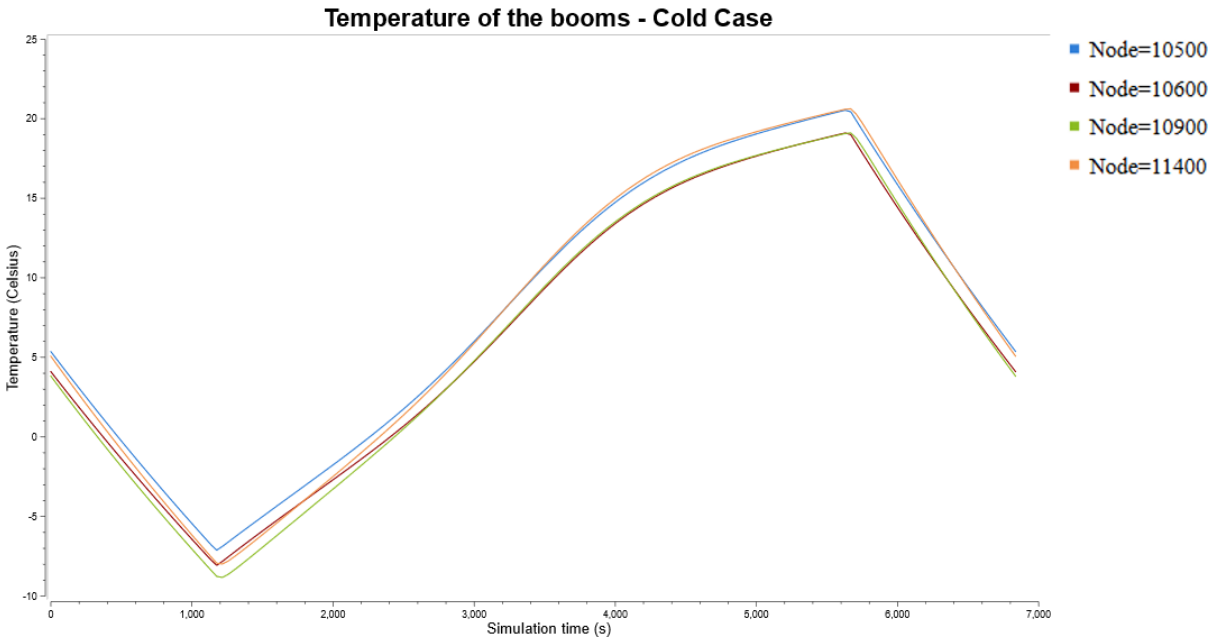

Figure 4.11: Time dependence of temperature of the booms when an equilibrium is reached in the cold case scenario. Table 4.1 provides a reference for the correspondence between shapes and nodes.

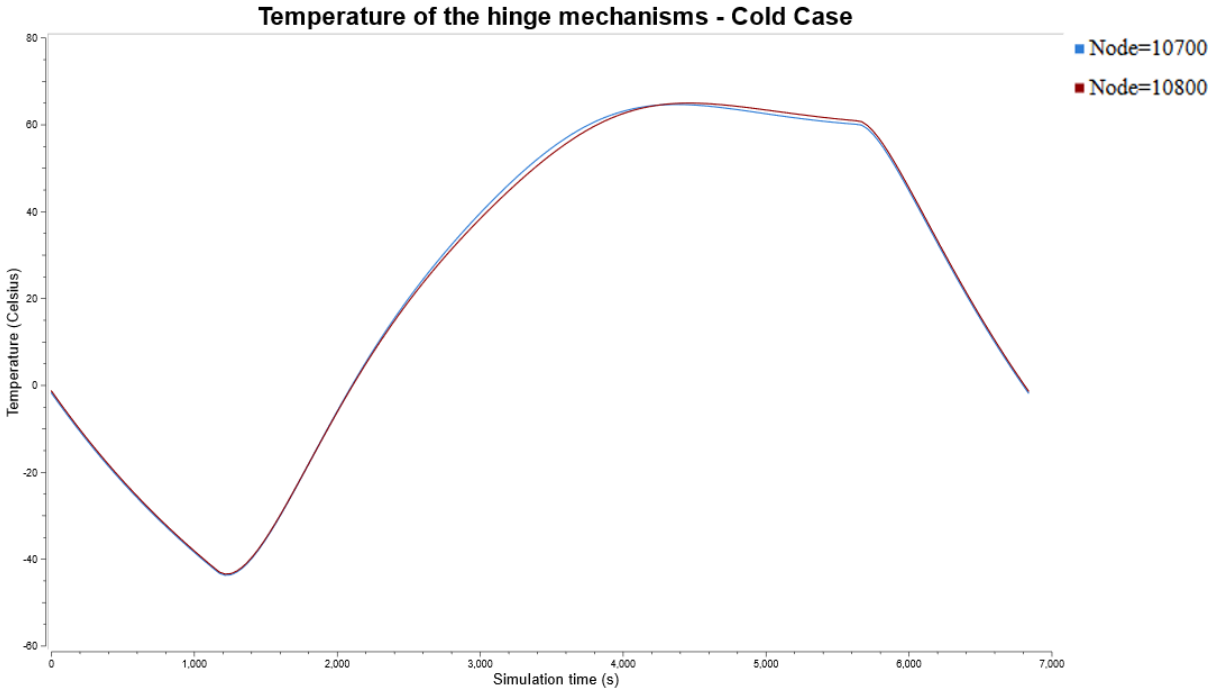

Figure 4.12: Time dependence of temperature of the hinge mechanisms when an equilibrium is reached in the cold case scenario. Table 4.1 provides a reference for the correspondence between shapes and nodes.

Element	Node	Min Temperature (°C)
Left boom	10500	-7.1
Right boom	10600	-8.1
Left Hinge	10700	-43.7
Right Hinge	10800	-43.4
Interactive disc right bottom	10900	-8.8
Interactive disc left bottom	11400	-8.0
Probe left	11000	-7.1
Probe right	11100	-8.1
Interactive disc left top	11200	-7.1
Interactive disc right top	11300	-8.1

Table 4.3: Minimum temperature reached by each node of the Langmuir Probes during the cold case.

The time dependence of the absorbed solar and albedo fluxes, which takes into account the direct solar flux and the properties defined for each object, can be observed respectively in Figure 4.13 and Figure 4.14. They are zero at the beginning and end of the orbit, as the satellite is in Earth's umbra during those phases. Some nodes exhibit the same time dependence of temperature and have therefore been omitted from the plot to improve readability: node 10600 behaves similarly to 10500, 10800 to 10700, and 11100 to 11000.

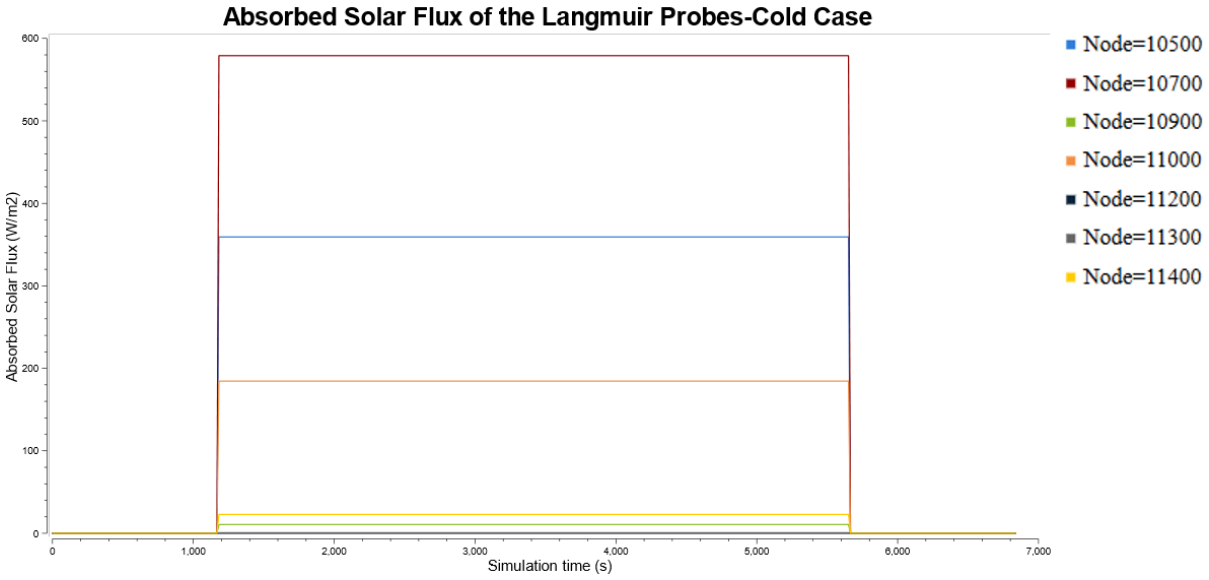

Figure 4.13: Time dependence of the solar absorbed flux of the Langmuir Probes in the cold case scenario. Table 4.1 provides a reference for the correspondence between shapes and nodes.

The time dependence of the absorbed IR flux, which takes into account the direct infrared flux and the properties defined for each object, can be observed in Figure 4.15

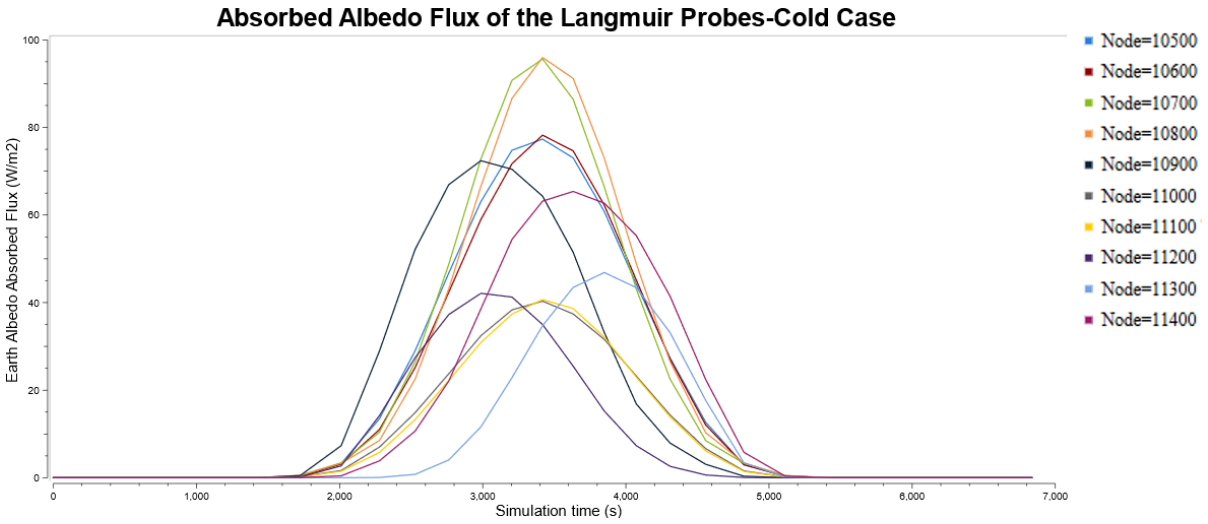

Figure 4.14: Time dependence of the albedo absorbed flux of the Langmuir Probes in the cold case scenario. Table 4.1 provides a reference for the correspondence between shapes and nodes.

and Figure 4.16. In this scenario, the nodes do not reach their peak simultaneously because the satellite's pointing is dynamic and continuously adjusted, causing different components to experience peak infrared radiation at different times.

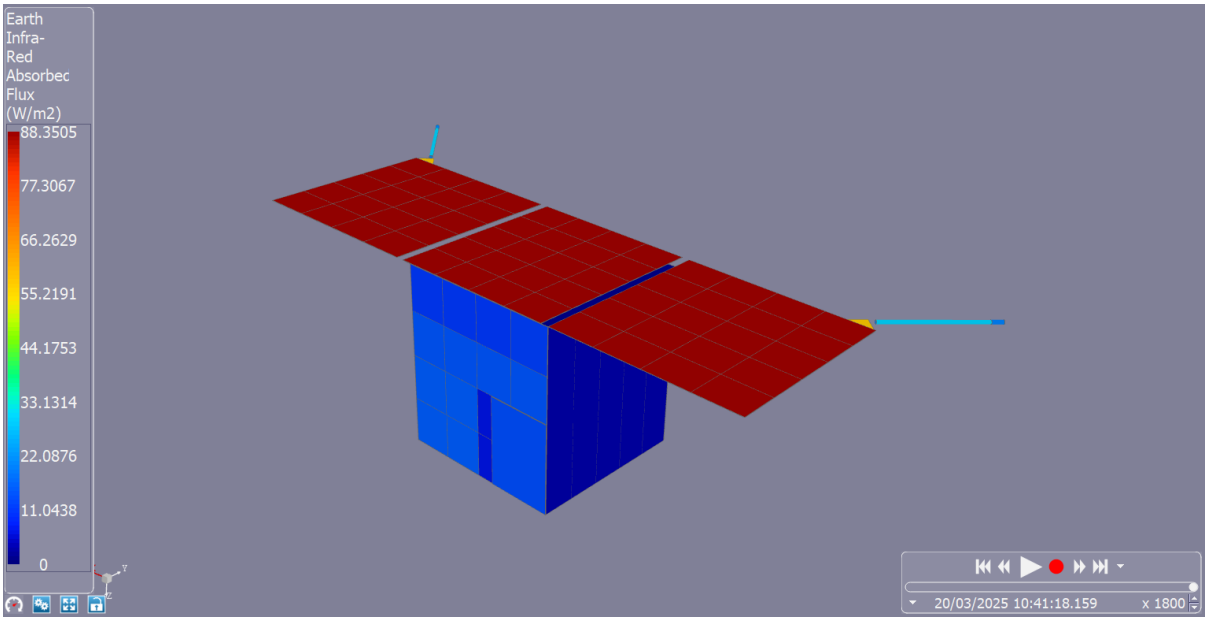

Figure 4.15: IR absorbed flux on the Langmuir Probes model at the end of the simulation time in the cold case scenario.

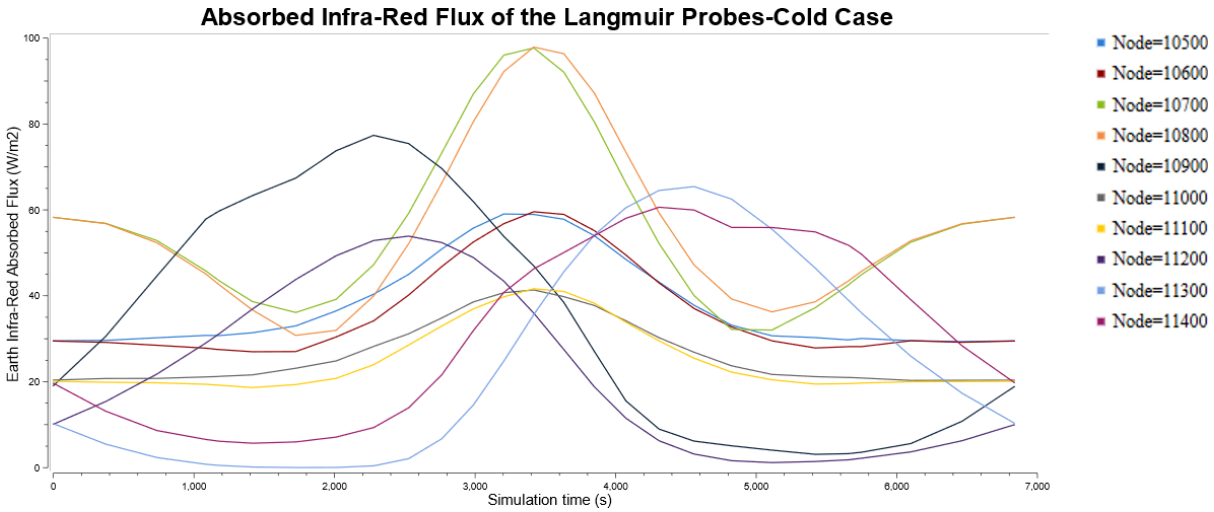

Figure 4.16: Time dependence of the IR absorbed flux of the Langmuir Probes in the cold case scenario. Table 4.1 provides a reference for the correspondence between shapes and nodes.

4.2 Langmuir Electronics Results

Assuming that the right side faces the tank and the front side faces the front plate, and using Figure 3.3 as a reference, the three Langmuir electronics boxes are numbered from 1 (bottom) to 3 (top). Table 4.4 provides a reference for interpreting the graphs, indicating which nodes correspond to each specific part of the electronics boxes.

Element	Node
Side face left (1)	6000
Side face left (2)	6001
Side face left (3)	6002
Bottom face	6100
Front face (1)	6200
Front face (2)	6201
Front face (3)	6202
Side face right (3)	6300
Side face right (2)	6301
Side face right (1)	6302
Back face (1)	6400
Back face (2)	6401
Back face (3)	6402
Top face	6500

Table 4.4: Correspondence between Langmuir Electronics elements and simulation nodes.

4.2.1 Hot Case

In the hot case scenario, the temperature results can be observed in Figure 4.17.

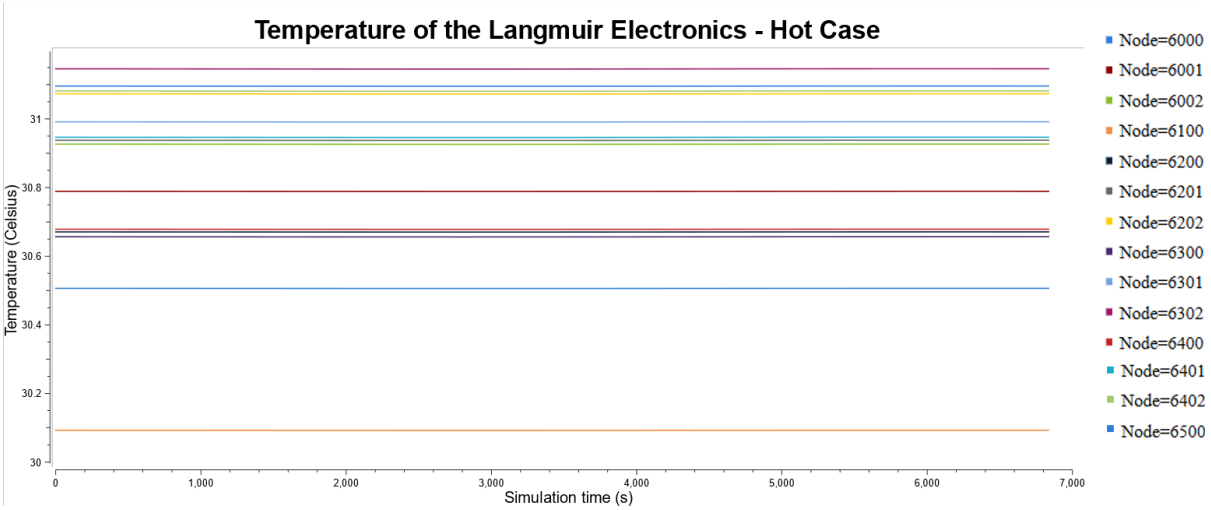

Figure 4.17: Time dependence of temperature of the Langmuir Electronics when an equilibrium is reached in the hot case scenario. Table 4.4 provides a reference for the correspondence between shapes and nodes.

The maximum temperature reached by each node is reported in Table 4.5. The temperature variation across the nodes is minimal. It primarily follows the imposed boundary condition of 29°C from the surrounding plates, with a slight increase due to internal power dissipation. The operational range, shown in Table 2.1, is respected.

Element	**Node**	**Max Temperature** (°C)
Side face left (1)	6000	30.5
Side face left (2)	6001	30.8
Side face left (3)	6002	30.9
Bottom face	6100	30.1
Front face (1)	6200	30.7
Front face (2)	6201	30.9
Front face (3)	6202	31.1
Side face right (3)	6300	30.7
Side face right (2)	6301	31.0
Side face right (1)	6302	31.1
Back face (1)	6400	30.7
Back face (2)	6401	30.9
Back face (3)	6402	31.1
Top face	6500	31.1

Table 4.5: Maximum temperature reached by each node of the Langmuir Electronics during the hot case.

4.2.2 Cold Case

In the cold case scenario, the temperature results can be observed in Figure 4.18.

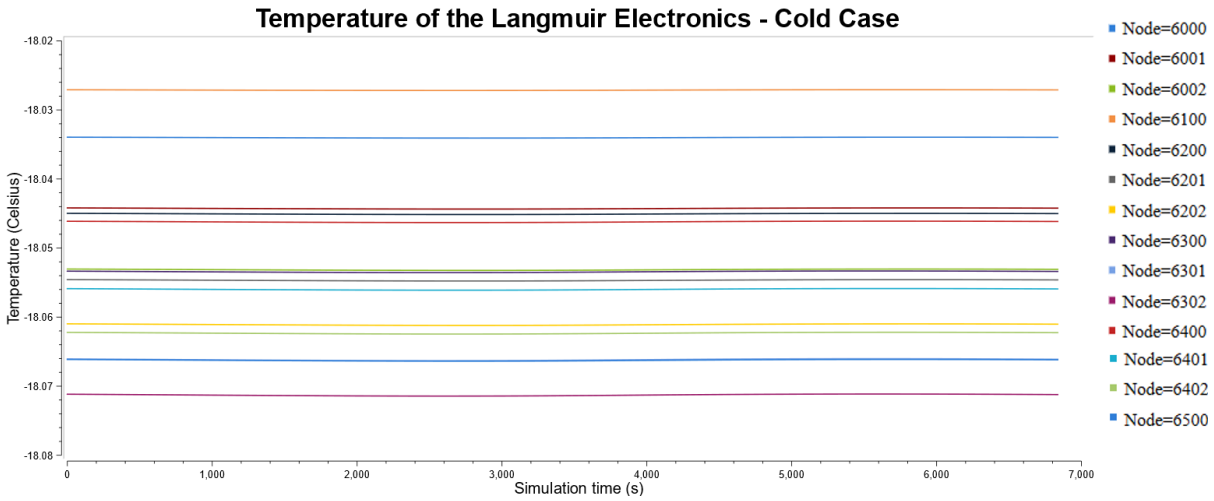

Figure 4.18: Time dependence of temperature of the Langmuir Electronics when an equilibrium is reached in the cold case scenario.Table 4.4 provides a reference for the correspondence between shapes and nodes.

The minimum temperature reached by each node is reported in Table 4.6. As in the hot case, the temperature variation across the nodes is minimal. It primarily follows the imposed boundary condition of -18 °C from the surrounding plates. The operational range, shown in Table 2.1, is respected.

Element	**Node**	**Min Temperature** (°C)
Side face left (1)	6000	-18.0
Side face left (2)	6001	-18.0
Side face left (3)	6002	-18.1
Bottom face	6100	-18.0
Front face (1)	6200	-18.0
Front face (2)	6201	-18.1
Front face (3)	6202	-18.1
Side face right (3)	6300	-18.1
Side face right (2)	6301	-18.1
Side face right (1)	6302	-18.1
Back face (1)	6400	-18.0
Back face (2)	6401	-18.1
Back face (3)	6402	-18.1
Top face	6500	-18.1

Table 4.6: Minimum temperature reached by each node of the Langmuir Electronics during the cold case.

4.3 Results Validation

To validate the numerical results and verify their physical consistency, a simplified analytical calculation was performed. The analysis focused on the hot case scenario, corresponding to a solar flux of 1428 W/m², where temperature variations are limited and an average steady-state value can be assumed. The boom was selected as the reference element for this check, as it is relatively isolated from the rest of the structure and less affected by conductive interactions.

The validation was based on the Stefan–Boltzmann law (Equation (2.14)). The absorbed contributions from solar flux, albedo, and IR were included using the values reported in Table 3.10. To better approximate the simulation conditions, the boom was assumed to be oriented perpendicular to both the Sun and the Earth.

The temperature obtained from the thermal simulation was approximately 39 °C. In contrast, the theoretical equilibrium temperature calculated using the thermal balance equation gives

$$T = \left(\frac{[(Q_s + Q_a) \cdot \alpha + Q_{ir} \cdot \varepsilon] \cdot A_a}{\sigma \varepsilon A_e} \right)^{1/4} = 66^{\circ}\mathrm{C} \tag{4.1}$$

where α and ε are the absorptivity and emissivity of the boom material, as listed in Table 3.4, A_a is the projected area exposed to incoming radiation (absorptance area), while A_e represents the lateral surface area of the boom responsible for the emission (emittance area).

The discrepancy between the simulated and theoretical temperatures can be attributed to several factors. First, the theoretical computation assumes fluxes at standard conditions and does not account for the satellite's orbital altitude, which affects the actual incident flux values, particularly for IR and albedo. Second, albedo is a diffuse and scattered component, and its spatial distribution is difficult to model accurately in a simplified analytical context, especially when estimating the fraction effectively reaching the boom. Therefore, while the theoretical estimate offers a reasonable approximation for comparison, its validity depends on the simplifications and assumptions adopted in the calculation. To obtain more accurate and consistent results, the simulation should be carried out under the exact same conditions assumed in the theoretical analysis.

4.4 Comparison

To evaluate the impact of the model simplification, the results have been compared with those obtained from the full satellite simulation previously developed by the University of Stuttgart, which model is illustrated in Figure 3.1. Table 4.7 and Table 4.8 help to interpret the graphs by indicating which nodes correspond to which part of the instrument they represent, considering the full satellite previously developed by the University of Stuttgart.

Element	Node
Left boom	10500
Right boom	10600
Left Hinge	10700
Right Hinge	10800
Interactive disc right bottom	11000
Interactive disc left bottom	11200
Interactive disc left top	11100
Interactive disc right top	10900

Table 4.7: Correspondence between Langmuir probe elements and simulation nodes, considering the mesh previously developed by the University of Stuttgart.

Element	Node
Side face right	6000
Back face	6100
Side face right	6200
Front face	6300
Top face	6400
Bottom face	6500

Table 4.8: Correspondence between Langmuir Electronics elements and simulation nodes, considering the mesh previously developed by the University of Stuttgart..

4.4.1 Langmuir Probes Simulation

The absorbed solar, albedo, and IR fluxes show similar time dependence in both the full and simplified models, being primarily determined by the physical properties of the components and the orbital trajectory and planet's properties.

Regarding the thermal results, the temperature of the Langmuir Probes in the hot case shows a similar overall time evolution in both configurations, with differences at each node remaining below 1 °C. The results of the full model are presented in Figure 4.19

and Figure 4.20, demonstrating good agreement with the simplified model results shown in Figure 4.2 and Figure 4.3. This small variation is considered acceptable and is primarily due to the surrounding simplified geometry and the inclusion of the Langmuir probe geometry itself, modeled as an aluminum element at the end of the boom, which is absent in the preliminary simulation.

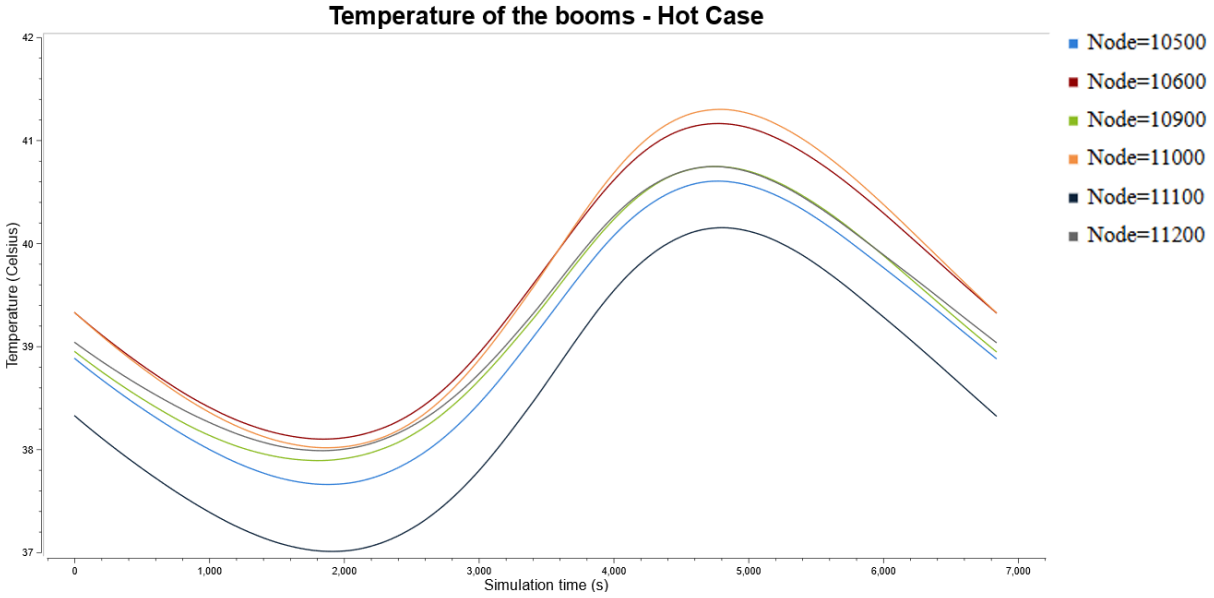

Figure 4.19: Time dependence of temperature of the booms when an equilibrium is reached in the hot case scenario, considering the simulation previously developed by the University of Stuttgart. Table 4.7 provides a reference for the correspondence between shapes and nodes.

In the cold case, however, the behavior differs more significantly. The absence of the physical geometry of the Langmuir probe at the tip of the boom appears to play a more relevant role in this thermal scenario. A dedicated simulation was conducted using the simplified model but without the probe: in this case, the temperature difference concerning the complete simulation is reduced to 2–4 °C. This deviation can reasonably be attributed to the absence of surrounding cold structures and their reflective contributions in the simplified geometry. However, when the probe is included in the simplified model, the temperature difference increases to approximately 10 °C. The results of the full model are presented in Figure 4.21 and Figure 4.22, showing a slight discrepancy with the simplified model results shown in Figure 4.11 and Figure 4.12. This is explained by the radiative and conductive effects introduced by the probe geometry. The aluminum probe, due to its thermal properties and position, alters the heat exchange at the end of the boom, potentially reducing its radiative efficiency, which results in an overall temperature increase that

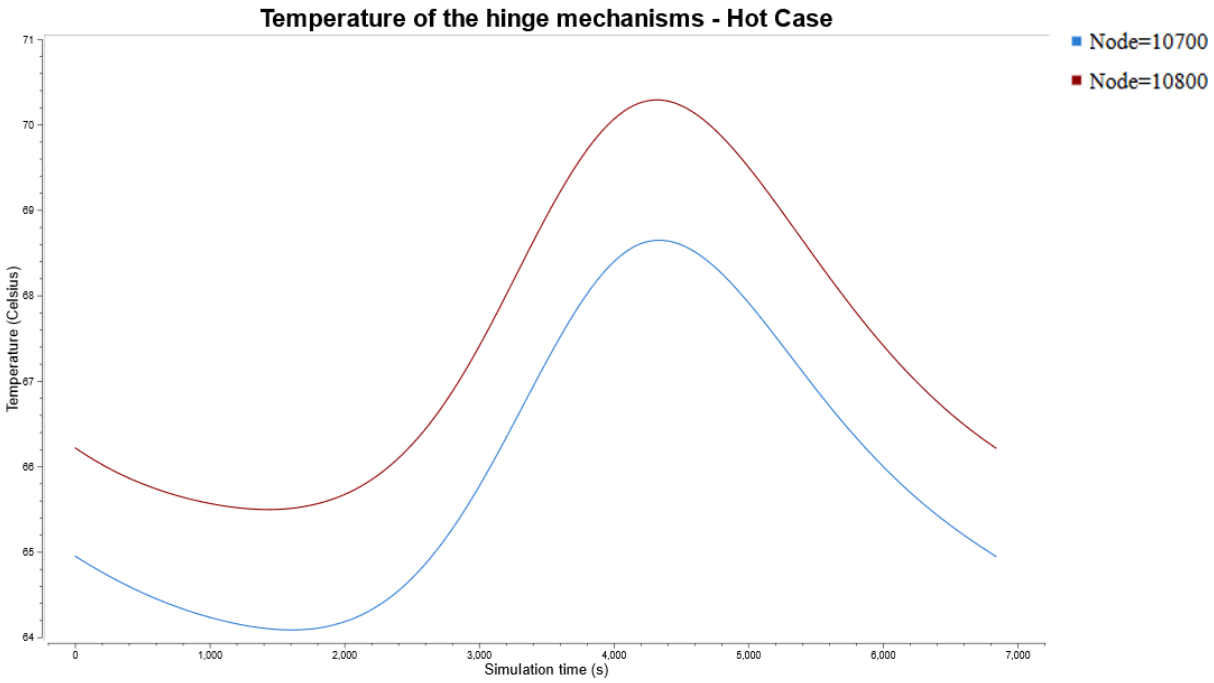

Figure 4.20: Time dependence of temperature of the hinge mechanisms when an equilibrium is reached in the hot case scenario, considering the simulation previously developed by the University of Stuttgart. Table 4.7 provides a reference for the correspondence between shapes and nodes.

is not observed in the full model. In support of this interpretation, it is worth noting that the hinge mechanisms exhibit a similar time dependence of temperature in both configurations, with minimal temperature differences, around 1 °C for the minimum temperature, suggesting that the observed temperature increase is primarily linked to the effects introduced by the probe geometry.

4.4.2 Langmuir Electronics Simulation

In the hot case, the simulation results of the simplified Langmuir electronics model are consistent with those obtained from the full satellite model. The resulting temperature is close to that of the surrounding plates, approximately 20 °C, as shown in Figure 4.23.

Similarly, in the cold case, the results of the complete model align well with the results of the simplified model ones, remaining close to the imposed boundary conditions, with a temperature difference of only 1–2 °C, as shown in Figure 4.24. This behavior can be attributed to the nature of the thermal interactions in the two scenarios. In the hot case, the electronic box is limited in dissipating excess heat, and thus tends to follow the temperature of the surrounding plates. In the cold case, however, the box

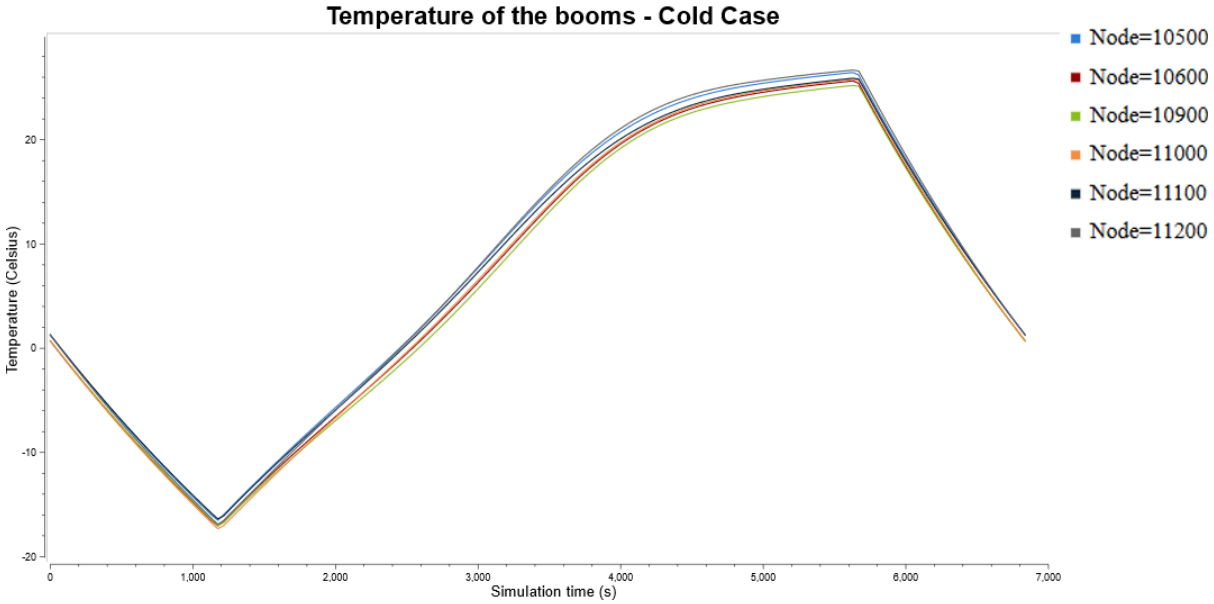

Figure 4.21: Time dependence of temperature of the booms when an equilibrium is reached in the cold case scenario, considering the simulation previously developed by the University of Stuttgart. Table 4.7 provides a reference for the correspondence between shapes and nodes.

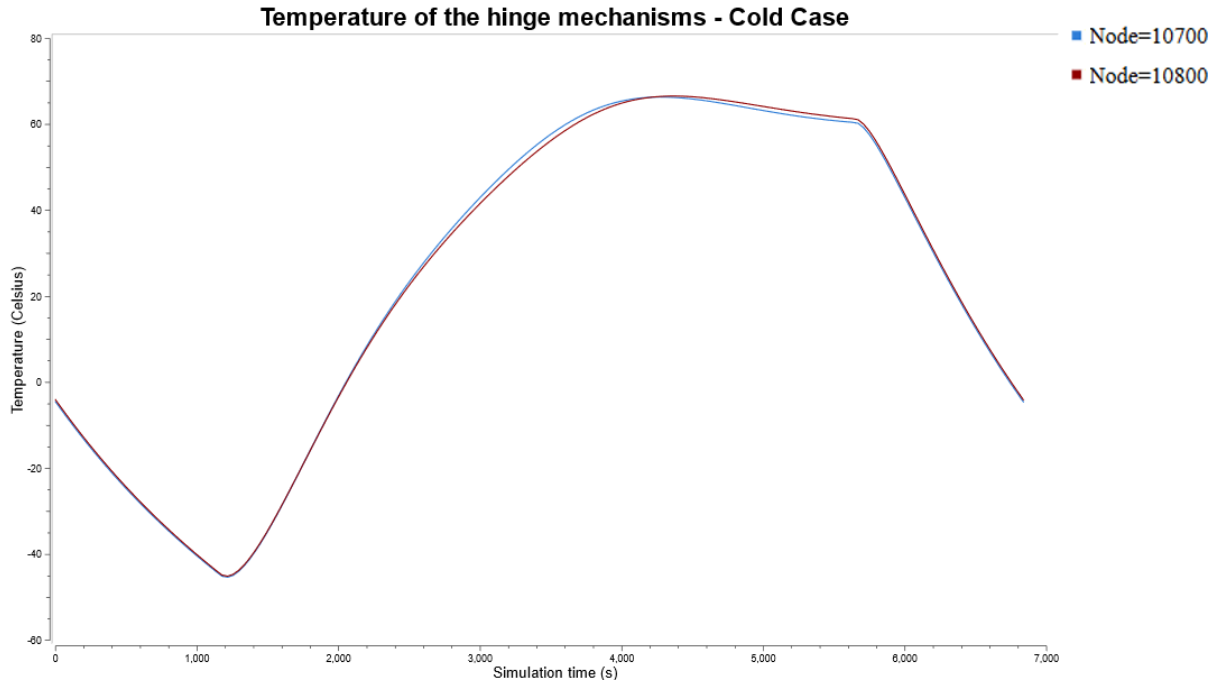

Figure 4.22: Time dependence of temperature of the hinge mechanisms when an equilibrium is reached in the cold case scenario, considering the simulation previously developed by the University of Stuttgart. Table 4.7 provides a reference for the correspondence between shapes and nodes.

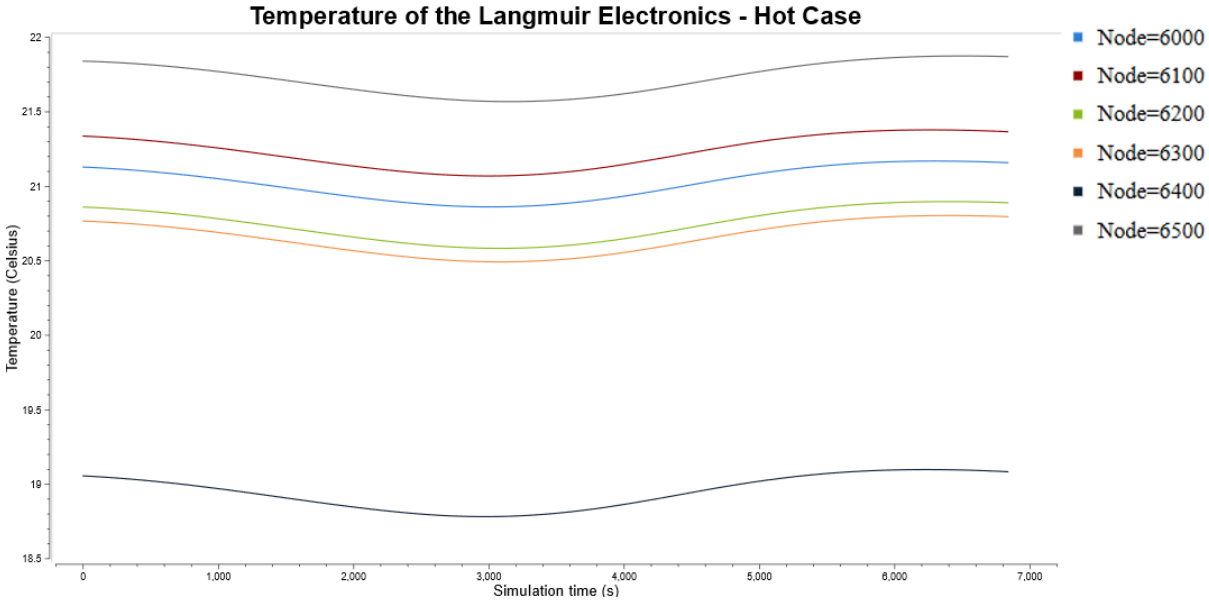

Figure 4.23: Time dependence of the temperature of the Langmuir Electronics when an equilibrium is reached in the hot case scenario, considering the simulation previously developed by the University of Stuttgart. Table 4.8 provides a reference for the correspondence between shapes and nodes.

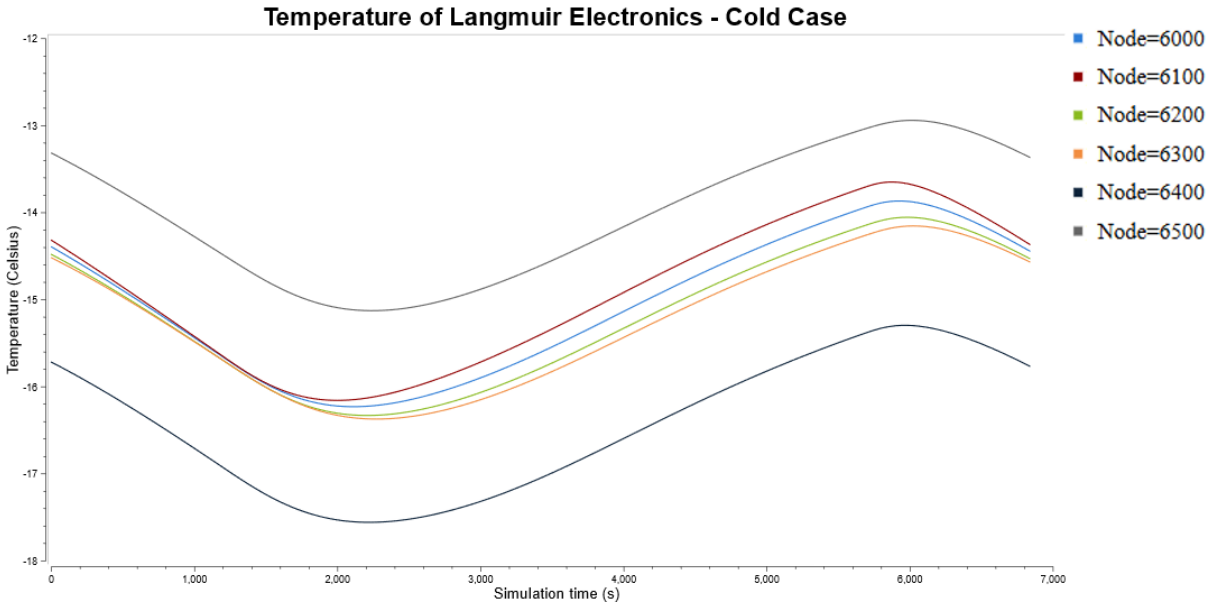

Figure 4.24: Time dependence of the temperature of the Langmuir Electronics when an equilibrium is reached in the cold case scenario, considering the simulation previously developed by the University of Stuttgart. Table 4.8 provides a reference for the correspondence between shapes and nodes.

remains warmer than the fixed boundary conditions of the simplified model, likely due to the influence of other nearby components that contribute additional heat through conduction or radiation. Furthermore, differences in the position and geometry of the box between the simplified and the complete models may also have contributed to the observed variations.

Chapter 5

Updated version of the ROMEO satellite

This chapter presents the updated version of the ROMEO satellite. The corresponding thermal simulations are carried out and compared with the results obtained from the previous configuration.

5.1 Model updates

In parallel with this work, the University of Stuttgart implemented the updated version of the ROMEO satellite in the Systema-Thermica software, shown in Figure 5.1. The main differences in this model include a larger solar panel and an expanded structural design, which incorporates the addition of brackets.

Consistent with the previous work, the same methodology has been applied to this model. Accordingly, two simplified models were developed: one representing the Langmuir probes and another for the associated electronics, as illustrated in Figure 5.2.

Several updates have been implemented in the Langmuir Probe model, including an increased boom length of up to 0.420 m and an updated thickness of both the boom and the probes to 0.001 m.

For the Langmuir Electronics, different power dissipation values, 5 W, 10 W, and 15 W, were considered to assess their impact on the thermal results.

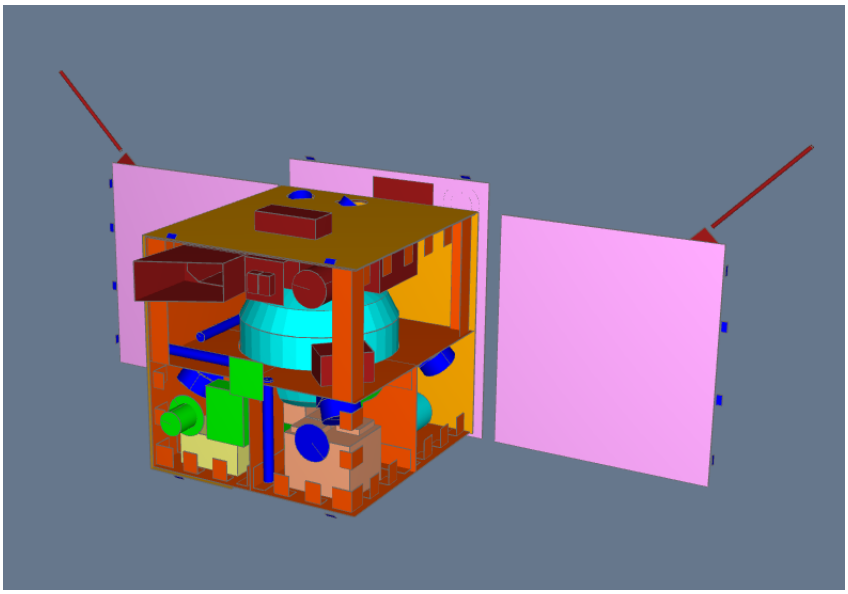

Figure 5.1: Updated model of the ROMEO satellite provided by the University of Stuttgart.

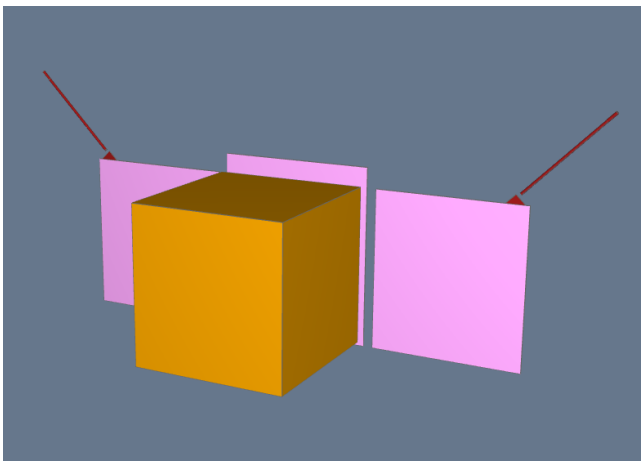

(a) Langmuir probes model.

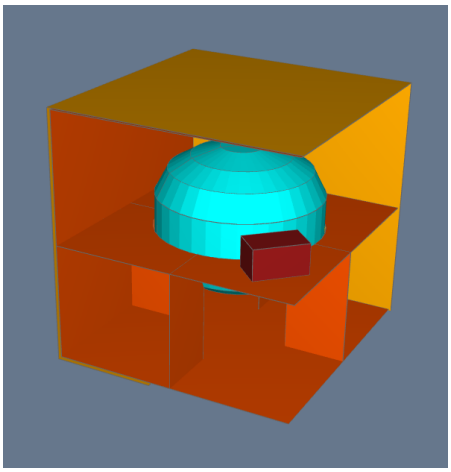

(b) Langmuir electronics model.

Figure 5.2: Langmuir instrument updated model.

5.2 Langmuir Probes Results

5.2.1 Hot Case

In the hot case scenario, the temperature time dependence of temperature for the updated booms is presented in Figure 5.3, while the results for the hinge mechanism are reported in Figure 5.4. Due to the solid mechanical connection, nodes 11000 and 11200 follow the same time dependence of temperature as node 10500, while nodes 11100 and 11300 follow the time dependence of temperature of node 10600. For good readability, they have not been plotted.

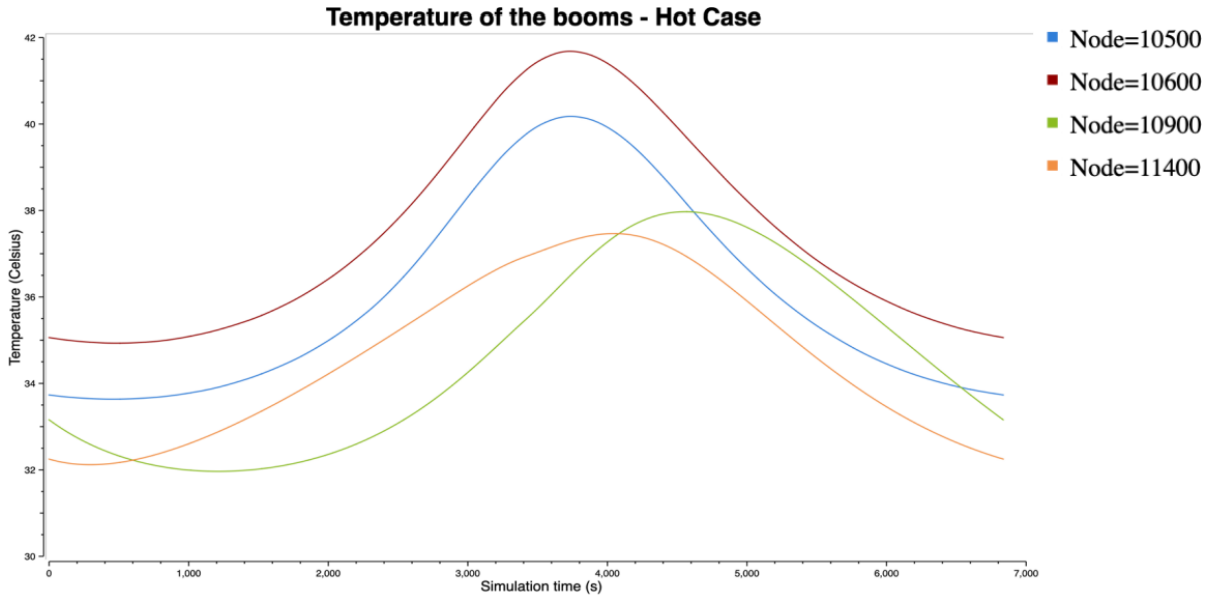

Figure 5.3: Time dependence of temperature of the updated booms when an equilibrium is reached in the hot case scenario. Table 4.1 provides a reference for the correspondence between shapes and nodes.

The maximum temperature reached by each node is reported in Table 5.1. The booms' results show a slight increase relative to those obtained with the previous simplified Langmuir Probe model shown in Table 4.2, while the hinge mechanisms show a slight decrease. The operational range, shown in Table 2.1, is respected. No significant variations are observed in the absorbed solar, albedo, and IR fluxes compared to the previous simplified model.

5.2.2 Cold Case

In the cold case scenario, the temperature time dependence of temperature for the updated booms is presented in Figure 5.5, while the results for the hinge mechanism

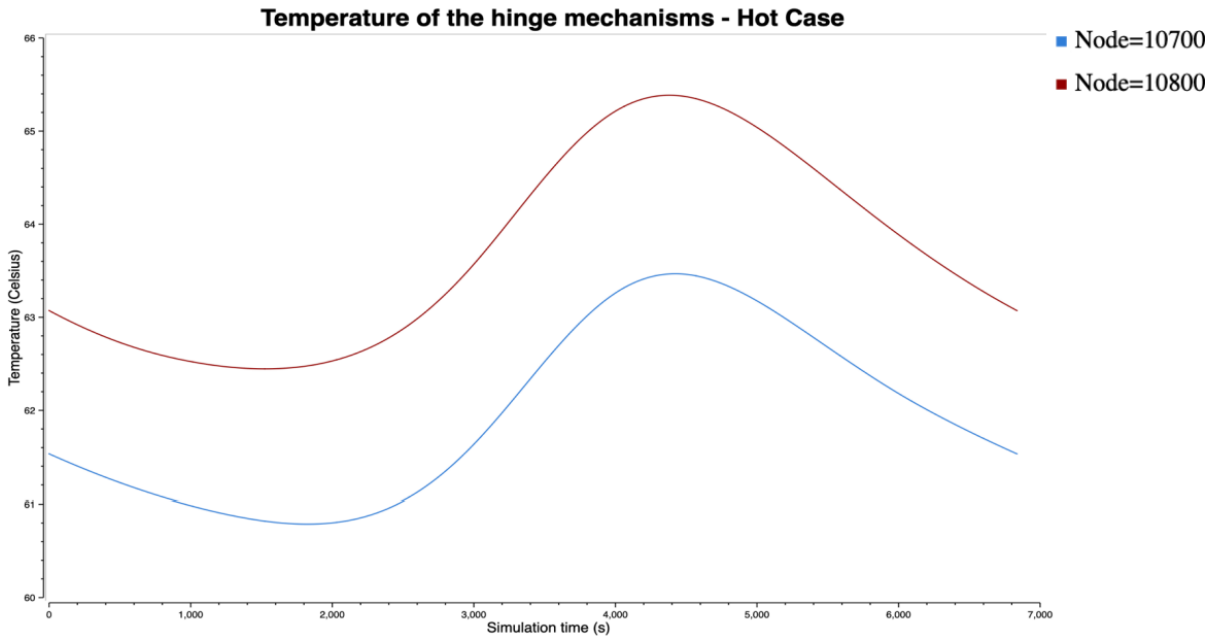

Figure 5.4: Time dependence of temperature of the hinge mechanisms when an equilibrium is reached in the hot case scenario. Table 4.1 provides a reference for the correspondence between shapes and nodes.

Element	**Node**	**Max Temperature** (°C)
Left boom	10500	40.2
Right boom	10600	41.7
Left Hinge	10700	63.5
Right Hinge	10800	65.4
Interactive disc right bottom	10900	38.0
Interactive disc left bottom	11400	37.5
Probe left	11000	40.2
Probe right	11100	41.7
Interactive disc left top	11200	40.1
Interactive disc right top	11300	41.6

Table 5.1: Maximum temperature reached by each node of the updated Langmuir Probes during the hot case.

are reported in Figure 5.6. Due to the solid mechanical connection, the probes likely follow the same temperature time dependence of temperature as the booms. For clarity, nodes 11000, 11100, 11200, and 11300 are not plotted, as nodes 11000 and 11100 show the same time dependence of temperature as node 10500, while nodes 11200 and 11300 follow the same behavior as node 10600.

The minimum temperature reached by each node is reported in Table 5.2. These values are particularly low for the booms and probes and fall below the operational range defined in Table 2.1, while the hinge mechanisms show an increase in temperature

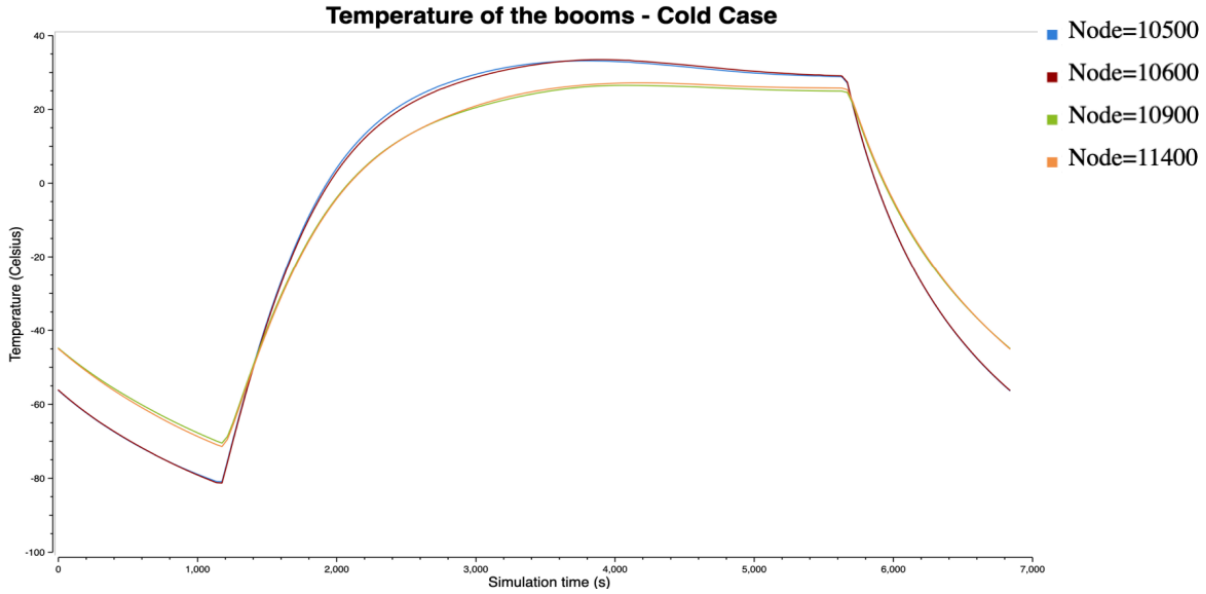

Figure 5.5: Time dependence of temperature of the updated booms when an equilibrium is reached in the cold case scenario. Table 4.1 provides a reference for the correspondence between shapes and nodes.

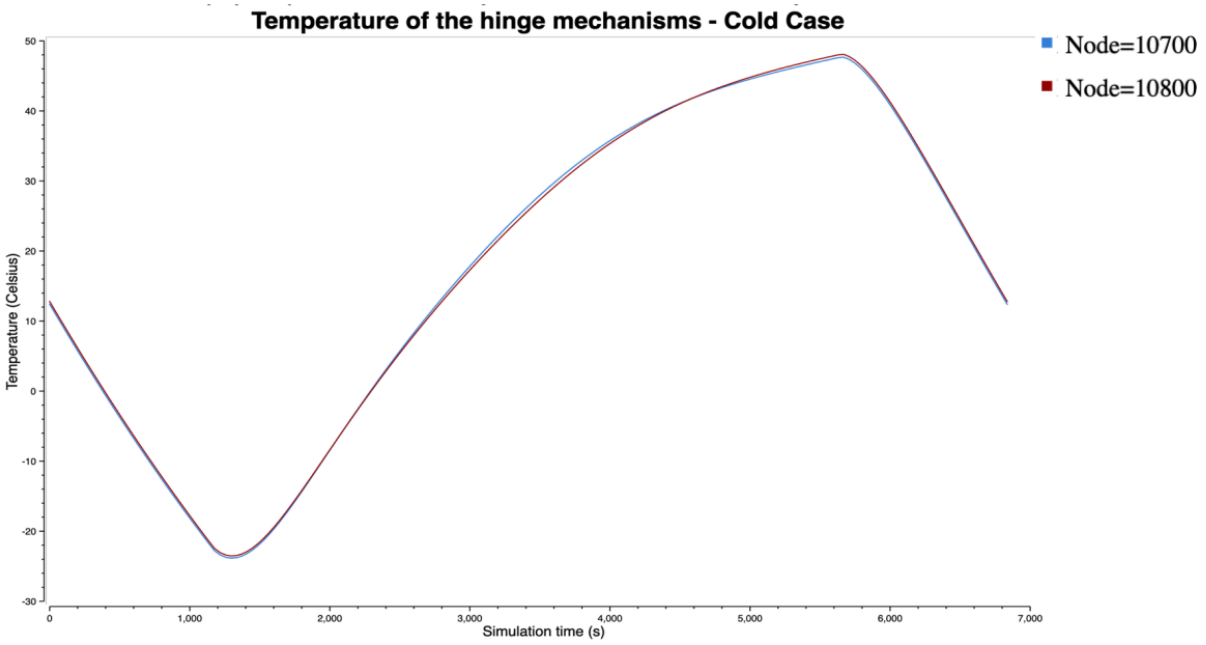

Figure 5.6: Time dependence of temperature of the hinge mechanisms when an equilibrium is reached in the cold case scenario. Table 4.1 provides a reference for the correspondence between shapes and nodes.

compared to the previous simplified Langmuir Probe model results, shown in Table 4.3. No significant variations are observed in the absorbed solar, albedo, and IR fluxes compared to the previous simplified model.

Element	**Node**	**Min Temperature** (°C)
Left boom	10500	-80.9
Right boom	10600	-81.3
Left Hinge	10700	-22.8
Right Hinge	10800	-22.4
Interactive disc right bottom	10900	-70.2
Interactive disc left bottom	11400	-71.2
Probe left	11000	-80.9
Probe right	11100	-81.2
Interactive disc left top	11200	-81.0
Interactive disc right top	11300	-81.4

Table 5.2: Minimum temperature reached by each node of the updated Langmuir Probes during the cold case.

5.3 Langmuir Electronics Results

No significant differences in the temperature results are observed compared to the previous simplified Langmuir Electronics model in the cold case and when the same dissipation of 5 W is applied. However, in the hot case, other dissipation values were analyzed to investigate their influence on the thermal performance.

5.3.1 10 W of dissipation

The maximum temperature reached by each node is reported in Table 5.3. It can be observed that, while the bottom face shows only a slight temperature increase, the other faces reach temperatures up to nearly 5 °C higher compared to the case with 5 W dissipation, which is shown in Table 4.5. The operational range, shown in Table 2.1, is respected.

5.3.2 15 W of dissipation

The maximum temperature reached by each node is reported in Table 5.4. It can be observed that, while the bottom face shows only a slight temperature increase, the other faces reach temperatures up to nearly 10 °C higher compared to the case with 5

Element	**Node**	**Max Temperature** (°C)
Side face left (1)	6000	35.7
Side face left (2)	6001	35.01
Side face left (3)	6002	33.9
Bottom face	6100	31.6
Front face (1)	6200	34.6
Front face (2)	6201	35.3
Front face (3)	6202	35.8
Side face right (3)	6300	34.4
Side face right (2)	6301	35.3
Side face right (1)	6302	35.9
Back face (1)	6400	34.6
Back face (2)	6401	35.3
Back face (3)	6402	35.8
Top face	6500	36.6

Table 5.3: Maximum temperature reached by each node of the Langmuir Electronics during the hot case, considering 10 W of dissipation.

W dissipation, which is shown in Table 4.5. The operational range, shown in Table 2.1, is respected.

Element	**Node**	**Max Temperature** (°C)
Side face left (1)	6000	39.0
Side face left (2)	6001	37.9
Side face left (3)	6002	36.3
Bottom face	6100	32.8
Front face (1)	6200	37.3
Front face (2)	6201	38.4
Front face (3)	6202	39.1
Side face right (3)	6300	37.0
Side face right (2)	6301	38.4
Side face right (1)	6302	39.3
Back face (1)	6400	37.3
Back face (2)	6401	38.4
Back face (3)	6402	39.1
Top face	6500	40.2

Table 5.4: Maximum temperature reached by each node of the Langmuir Electronics during the hot case, considering 15 W of dissipation.

Chapter 6

Conclusion

This thesis has presented a thermal analysis of the Langmuir instrument onboard the ROMEO satellite, based on a simplified modeling approach. The results indicate that the adopted methodology is valid in specific scenarios, as long as the underlying assumptions and simplifications are properly acknowledged.

A key limitation of the approach lies in its lack of general applicability: each simplified model requires validation against a full satellite simulation to ensure consistency and accuracy. Therefore, while the method proves effective in reducing computational time, it must always be used with caution and in conjunction with thorough verification.

The methodology could be further validated through cross-validation using other thermal analysis software, and future developments may include experimental testing of the Langmuir Probe instrument to assess how accurately the simulation reflects the actual thermal behavior of the instrument. Furthermore, the thermal model could be improved by introducing more detailed geometries and refining the treatment of internal power dissipation, which in this work was not finalized yet in value and distribution.

In addition, it would be valuable to investigate the thermal behavior of the Langmuir Probe under alternative mission scenarios, such as the stowed configuration before deployment.

While addressing strategies to prevent the Langmuir booms and probes from falling outside their defined operational temperature range was beyond the scope of this

thesis, it is worth noting that in the updated ROMEO model, they do drop below this range during the cold case. This highlights the need for further investigation, either to extend the acceptable temperature limits or to implement suitable thermal control strategies to ensure operational reliability.

With further validation and refinement, the approach developed in this report may serve as a valuable tool in future satellite thermal design. It enables the thermal behavior of specific components to be analyzed independently, thereby significantly reducing computational effort without compromising accuracy

Bibliography

[1] Airbus Defence and Space. *SYSTEMA V4.9 User Guide*. 2022.

[2] Airbus Defence and Space. *Thermica V4.9 User Guide*. 2023.

[3] Airbus Defence and Space. *Thermisol V4.9 User Guide*. 2022.

[4] Berggren, Andreas. "Design of Thermal Control System for the Spacecraft MIST". MA thesis. KTH Royal Institute of Technology, 2015.

[5] Bjornberg, Anton and Larsson, Erik. *Thermal Analysis and Control of MIST*. 2017.

[6] Chandrashekar, Shreyas. *Thermal Analysis and Control of MIST CubeSat*. Feb. 2017.

[7] Gilmore, David G. *Spacecraft Thermal Control Handbook: Fundamental Technologies*. The Aerospace Press, 2002.

[8] Hoffman, Richard H. "Spaceflight Performance of Silver-Coated FEP Teflon as a Thermal Control Surface on the IMP-1 Spacecraft". In: *NASA Goddard Space Flight Center Technical Report* (1973).

[9] Käufl, Antonie. "Development of the Thermal Concept for the Small Satellite ROMEO". MA thesis. University of Stuttgart, Sept. 2023.

[10] Lengowski, Michael. "Entwicklung mechanisch/thermischer Architekturen und innovativer Strukturelemente im Rahmen zweier Satellitenmissionen des Stuttgarter Kleinsatellitenprogramms". PhD thesis. Universität Stuttgart, Institut für Raumfahrtsysteme, 2013.

[11] Oliveira Nogueira, Pedro Henrique de. "Micro-Satellite Electrical Power Subsystem Design and Test for LEO Mission". MA thesis. Instituto Nacional de Pesquisas Espaciais (INPE), 2017.

[12] Paraschiv, Lizica Simona et al. “A Web Application for Analysis of Heat Transfer Through Building Walls and Calculation of Optimal Insulation Thickness”. In: *Energy and Buildings* (2020).

[13] Prokhorov, Alexander. “Theoretical Basis of Blackbody Radiometry”. In: *Journal of Radiometric Studies* (Oct. 2020).

[14] University of Stuttgart, Institute of Space Systems. *ROMEO Small Satellite Program*. Available at: `https://www.irs.uni-stuttgart.de/en/research/satellitetechnology-and-instruments/smallsatelliteprogram/romeo/`.

[15] Yusufoglu, Ufuk Alper et al. “Simulation of Energy Production by Bifacial Modules with Revision of Ground Reflection”. In: *Solar Energy Journal* (2014).